TAC+: Optimizing Error-Bounded Lossy Compression for 3D AMR Simulations

Daoce Wang[®], Jesus Pulido[®], Pascal Grosset[®], Sian Jin[®], Jiannan Tian[®], Kai Zhao[®], James Ahrens[®], and Dingwen Tao[®], *Senior Member, IEEE*

Abstract—Today's scientific simulations require significant data volume reduction because of the enormous amounts of data produced and the limited I/O bandwidth and storage space. Errorbounded lossy compression has been considered one of the most effective solutions to the above problem. However, little work has been done to improve error-bounded lossy compression for Adaptive Mesh Refinement (AMR) simulation data. Unlike the previous work that only leverages 1D compression, in this work, we propose an approach (TAC) to leverage high-dimensional SZ compression for each refinement level of AMR data. To remove the data redundancy across different levels, we propose several preprocess strategies and adaptively use them based on the data features. We further optimize TAC to TAC+ by improving the lossless encoding stage of SZ compression to handle many small AMR data blocks after the pre-processing efficiently. Experiments on 10 AMR datasets from three real-world large-scale AMR simulations demonstrate that TAC+ can improve the compression ratio by up to 4.9× under the same data distortion, compared to the stateof-the-art method. In addition, we leverage the flexibility of our approach to tune the error bound for each level, which achieves much lower data distortion on two application-specific metrics.

Index Terms—Data reduction, lossy compression, adaptive mesh refinement (AMR), scientific computing.

I. INTRODUCTION

He increase in supercomputer performance over the past decades has been insufficient to solve many challenging modeling and simulation problems. For example, the complexity of solving evolutionary partial differential equations scales as $\Omega(n^4)$, where n is the number of mesh points per dimension. Thus, the performance improvement of about three orders of magnitudes over the past 30 years has meant just a 5.6× gain in spatio-temporal resolution [1]. To address this issue, many high-performance computing (HPC) simulation packages [2] (such as AMReX [3] and Athena++ [4]) use Adaptive Mesh Refinement (AMR)—which applies computation to selective regions of most interest—to increase resolution. Compared to the method where a high resolution is applied everywhere, the AMR method greatly reduces the computational complexity and storage overhead; thus, it is one of the most widely used frameworks for many HPC applications [5]-[8].

Although AMR can save storage space to some extent, AMR applications running on supercomputers still generate large amounts of data, bringing challenges to data transmission and

Daoce Wang, Jiannan Tian, and Dingwen Tao (corresponding author) are with Indiana University, Bloomington, IN 47405, USA.

Jesus Pulido, Pascal Grosset, and James Ahrens are with Los Alamos National Laboratory, Los Alamos, NM 87545, USA.

Sian Jin is with Temple University, Philadelphia, PA 19122, USA. Kai Zhao is with Florida State University, Tallahassee, FL 32306, USA. storage. For example, one Nyx simulation [9] with a resolution of 4096^3 (i.e., 0.5×2048^3 mesh points in the coarse level and 0.5×4096^3 in the fine level) can generate up to 1.8 TB of data for a single snapshot; a total of 1.8 PB of disk storage is needed assuming running the simulation 5 times with 200 snapshots dumped per simulation. Therefore, reducing data size is necessary to lower the storage overhead and I/O cost and improve the overall application performance for running large-scale AMR simulations on supercomputers.

A straightforward way to address this issue is to use data compression. However, traditional lossless compression techniques such as GZIP [10] and Zstandard [11] can only provide a compression ratio by up to 2× for scientific data [12]. On the other hand, a new generation of lossy compressors that can provide strict error control (called "error-bounded" lossy compression) has been developed, such as SZ [13]–[15], ZFP [16], MGARD [17], [18], and TTHRESH [19]. Using those errorbounded lossy compressors, scientists can achieve relatively high compression ratios while minimizing the quality loss of reconstructed data and post-analysis, as seen in [20]–[27].

However, a gap exists between data compression and AMR data. The root of this disparity lies in the hierarchical nature of AMR data, where the entire dataset possesses varying resolutions/levels. Data at each level is sparse because it only covers a portion of the domain. Yet, current scientific compressors exclusively support the compression of non-sparse data with uniform resolution. Consequently, AMR data must be preprocessed prior to compression.

A straightforward pre-process would be to flatten the highdimensional AMR data from different levels into a 1D array for compression. However, this approach would cause the data to lose a significant amount of spatial information, which is critical for compression performance optimization.

To leverage high-dimension compression, a common approach is to generate uniform-resolution data by upsampling the coarse-level data and merging it with the finest-level data. However, this method introduces redundant information, which significantly reduces the compression ratio. This degradation is especially pronounced when the upsampling rate is high or when multiple coarse levels need to be upsampled. This presents us with a dilemma in compressing AMR data: we are forced to choose between losing spatial locality (by compressing in 1D) or introducing redundant information (by using upsampled 3D data).

Only a few existing contributions have investigated advanced error-bounded lossy compression for AMR applications and datasets. Recently, Luo *et al.* introduced zMesh [28], a tech-

nique that pre-processs the data by grouping data points that are mapped to the same or adjacent geometric coordinates such that the dataset is smoother and more compressible. However, since zMesh maps data points from different AMR levels to adjacent geometric coordinates and generates a 1D array, it still cannot adopt 3D compression which most HPC simulations use. Moreover, zMesh is designed for patch-based AMR data¹ and the reorganization approach proposed by zMesh cannot improve the data smoothness appropriately (see Section IV).

To solve these issues, we propose TAC that removes the redundant data in coarser level(s) and employs 3D lossy compression for each level. We note that each level may contain many empty/zero regions, where data points are saved in other levels, which may significantly decrease the data smoothness and hence reduce the compression ratio. To this end, TAC either removes these empty regions using adaptive partition strategies or partially pads them with appropriate values, based on the density of empty regions.

Another challenge is that the partition strategies can generate many (e.g., 3,000+) small data blocks, whereas the SZ compressor performs poorly on small data sets because of the Huffman encoding cost (will be detailed in Section III-D). TAC's solution to the heavy Huffman encoding cost is to linearize/merge the small blocks and then pass these merged blocks to SZ. This approach can reduce the cost of the Huffman encoding. However, TAC still faces a critical limitation: most of the merged small blocks are not adjacent in the original dataset, leading to rapid changes in the data values between these nonneighboring blocks, which can negatively impact the accuracy of SZ's predictor.

To address the limitations, we further optimize TAC to TAC+ by designing a Shared Huffman Encoding (SHE) approach for the SZ compressor. This approach allows individual predictions for each small block while being encoded using a single shared Huffman tree, which can improve the prediction accuracy and compression ratio accordingly.

The main contributions are summarized as follows.

- We propose to leverage 3D SZ compression to compress each level of an AMR dataset separately. We propose a hybrid compression approach based on the following three pre-process strategies and data characteristics.
- We propose an optimized sparse tensor representation to efficiently partition data and remove empty regions for sparse AMR data.
- We propose an enhanced k-d tree approach to reduce the time overhead of removing empty regions.
- We propose a padding approach to improve the smoothness and compressibility of dense AMR data.
- We employ the SHE approach in the SZ compressor to reduce the high time and storage costs of compressing multiple small blocks in order to achieve better compression on AMR data after the partition.
- We tune the error bound for each AMR level to further improve the compression quality in terms of two application-specific post-analysis metrics.

¹The patch-based AMR data redundantly saves the data block to be refined at the next finer level in the current coarse level (see Section II-C).

 Experiments show that, compared to the state-of-the-art approach zMesh, our proposed AMR compression can improve the compression ratio by up to 4.9× under the same data distortion on the tested datasets.

2

We evaluate our proposed compression method on ten datasets from three real-world AMR applications: Nyx [9], WarpX [29], and IAMR [30]. We compare our method with four baselines including zMesh using generic metrics such as compression ratio and peak signal-to-noise ratio (PSNR) and application-specific metrics such as power spectrum and halo finder. Our code is available at https://github.com/hipdac-lab/HPDC22-TAC.

The remaining paper is organized as follows. In Section II, we present background information about error-bounded lossy compression, AMR method, k-d tree, and related work on AMR data compression. In Section III, we describe our proposed preprocess strategies, SHE approach, and hybrid compression. In Section IV, we show the experimental results on different AMR datasets. In Section V, we conclude our work and discuss the future work.

II. BACKGROUND AND RELATED WORK

A. Lossy Compression for Scientific Data

There are two main categories for data compression: lossless and lossy compression. Compared to lossless compression, lossy compression can offer a much higher compression ratio by trading a little bit of accuracy [31]. There are some well-developed lossy compressors for images and videos such as JPEG [32] and MPEG [33], but they do not have a good performance on the scientific data because they are mainly designed for integers rather than floating points.

In recent years there is a new generation of lossy compressors that are designed for scientific data, such as SZ [13]-[15], ZFP [16], MGARD [17], and TTHRESH [19]. These lossy compressors provide parameters that allow users to finely control the information loss introduced by lossy compression. Unlike traditional lossy compressors such as JPEG [32] for images (in integers), SZ, ZFP, MGARD, and TTHRESH are designed to compress floating-point data and can provide a strict errorcontrolling scheme based on the user's requirements. Generally, lossy compressors provide multiple compression modes, such as error-bounding mode and fixed-rate mode. Error-bounding mode requires users to set an error type, such as the point-wise absolute error bound and point-wise relative error bound, and an error bound level (e.g., 10^{-3}). The compressor ensures that the differences between the original data and the reconstructed data do not exceed the user-set error bound level.

In this work, we focus on the SZ lossy compression (2021 R&D 100 Award Winner) because SZ typically provides a higher compression ratio than ZFP [23], [34] and higher speeds than MGARD [34], [35] and TTHRESH [19]. SZ is a prediction-based error-bounded lossy compressor for scientific data. It has three main steps: (1) predict each data point's value based on different prediction methods; (2) quantize the difference between the real value and predicted value based on the user-set error bound; and (3) apply a customized Huffman coding and lossless compression.

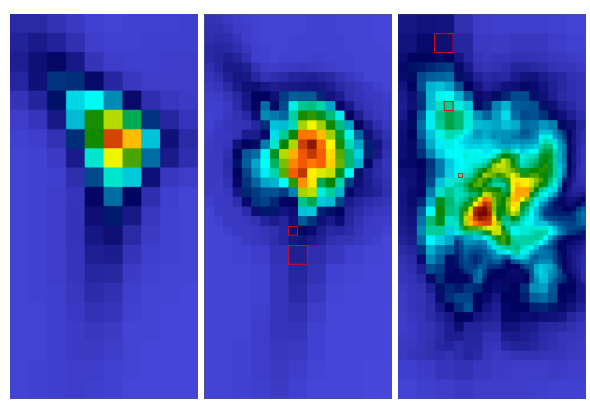


Fig. 1: Visualization (one zoom-in 2D slice) of three key timesteps generated from an AMR-based cosmology simulation. The grid structure changes with the universe's evolution. The red boxes indicate different resolutions within one AMR level

The SZ framework comprises a series of algorithms tailored to various user and application needs. In this study, we primarily focus on its two principal algorithms: the compression algorithm that utilizes the Lorenzo and linear regression predictors, denoted as "Lor/Reg" [15], and the compression algorithm based on the spline interpolation approach, denoted as "Interp" [34]. Specifically, the Lor/Reg method begins by truncating the entire input data into smaller blocks. It then applies either the Lorenzo predictor or the high-dimensional linear regression to each block separately. In contrast, the Interp algorithm carries out global interpolation across all three dimensions of the complete dataset. The Lor/Reg and Interp algorithms differ significantly, resulting in varied performance and features when compressing AMR data. A more in-depth discussion on this can be found in Sections III-D, III-E, and IV-E.

B. AMR Method and AMR Data

AMR is a method adapting the accuracy of a solution by using a non-uniform grid to increase computational and storage savings while still achieving the desired accuracy. AMR applications change the mesh or spatial resolution based on the level of refinement needed by the simulation and use *finer mesh in the regions with more importance/interest* and *coarser mesh in the regions with less importance/interest*. Figure 1 shows that the mesh will be refined when the value meets the refinement criteria, e.g., refining a block when its norm of the gradients or maximum value is larger than a threshold.

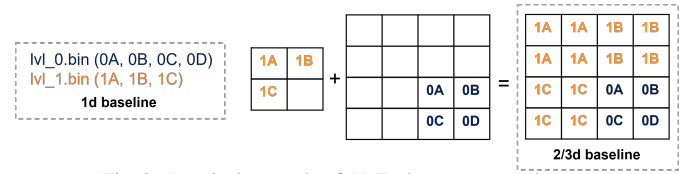


Fig. 2: A typical example of AMR data storage and usage.

Clearly, the data generated by an AMR application are hierarchical data with different resolutions. The data of each AMR level are usually stored separately (e.g., in a 1D array). For example, Figure 2 (left) shows a simple example of two-level AMR data; "0" means high resolution (the fine level) and "1" for low resolution (the coarse level). When the AMR data are needed for post analysis or visualization, users will typically

convert the data from different levels to a uniform resolution. In the previous example, we will up-sample the data at the coarse level and combine it with the data at the fine level, as shown in Figure 2 (right).

C. Tree-based and Patch-based AMR Data

There are two types of techniques to represent AMR data: patch-based AMR and tree-based AMR [36]. The main difference between them is that the patch-based AMR technique generates AMR data with redundancy across different levels. In other words, the patch-based AMR data structure redundantly saves data blocks to be refined at the next level in the current level, simplifying the computation in the refinement process. By comparison, the tree-based AMR technique organizes the grids on the tree leaves, so there is no redundant data across different levels. But tree-based AMR data is more complex for post analysis and visualization compared to patch-based AMR data [37], [38].

In this work, we focus on a state-of-the-art patch-based AMR framework AMReX. Note that since the redundant coarser-level data in the patch-based AMR will not often be used in post-analysis, we discard them during compression to improve the compression ratio.

D. Existing AMR Data Compression

1D AMR Compression: The main challenge for AMR data compression is that the AMR data is comprehensive and hierarchical with different resolutions. A naive approach is to compress the 1D data of each AMR level separately. However, this approach loses most of the topological/spatial information, which is critical for data compression. zMesh [28] is a stateof-the-art AMR data compression based on the 1D approach. Different from the naive 1D approach, zMesh re-organizes the 1D data based on each point's coordinate in the 2D layout; in other words, zMesh puts the points neighbored in the 2D layout closer in the 1D array. It can increase the data smoothness/compressibility to benefit the following 1D compression such as SZ on patch-based AMR data with redundancy across different AMR levels. However, zMesh does not leverage highdimensional compression, while many previous studies [14], [39], [40] proved that leveraging more dimensional information (e.g., spatial/temporal information) can significantly improve the compression performance. Moreover, it only focuses on 2D AMR data. Our work aims to leverage high-dimensional data compression and supports 3D AMR data.

High-dimensional AMR Compression: Similar to the idea described in Section II-B, a straightforward way to leverage 3D compression on 3D AMR data is to compress different levels together by up-sampling coarse levels. However, this approach must handle extra redundant data generated by the up-sampling process. As shown in Figure 2, 1A, 1B, and 1C are redundant points in the compression. Note that the storage overhead of these redundant points will be higher when more data are in the coarse levels or the up-sampling rate is higher, especially for 3D AMR data. This is because we only need to duplicate one point from the coarse level 4 times for 2D AMR data but 8 times for 3D AMR data, with an up-sampling

4

rate of 2. Another limitation of this approach is that it cannot apply different compression configurations (e.g., error bound) to different AMR levels. This is because after up-sampling all data points will have the same importance. However, the purpose of using the AMR method is to set different interests to different AMR levels, so the error bound for each AMR level can be chosen adaptively.

E. k-D Tree for Particle Data Compression

k-d tree [41] is a binary tree in which every node represents a certain space. Without loss of generality, for the 3D case, every non-leaf node in a k-d tree splits the space into two parts by a 2D plane associated with one of the three dimensions. The left subspace is associated with the left child of the node, while the right subspace is associated with the right child. k-d tree is commonly used in particle data compression [42]–[44] to locate each particle and remove empty regions. Specifically, a k-d tree keeps dividing the space in between along one dimension until the space is empty or contains only one particle. We will optimize the classic k-d tree and use it to remove empty regions and increase the compressibility for each AMR level (to be detailed in Section III-C).

III. OUR PROPOSED DESIGN

In this section, we introduce a compression framework tailored for AMR data, utilizing high-dimensional SZ lossy compression for each AMR level. Our initial proposal, TAC, integrates three pre-process strategies to address the challenges posed by irregular data distributions. Extending TAC, we present TAC+. In TAC+, we refine two pre-process methods from the original TAC and introduce Shared Huffman Encoding (SHE). We then integrate SHE with the Lor/Reg algorithm to bolster compression efficacy for AMR data. Furthermore, we propose adaptive approaches for TAC/TAC+, enabling the selection of the most suitable pre-process method based on each level's data density.

A. Ghost-Shell Padding for High-density Data

To compress the AMR data in 3D, besides the aforementioned 3D baseline, we can also compress each level separately in 3D. In that way, however, the data will be split into multiple levels, and each level will have many empty regions and an irregular data distribution, as shown in Figure 4. A naive solution to handle the irregular 3D data is to fill the empty regions with

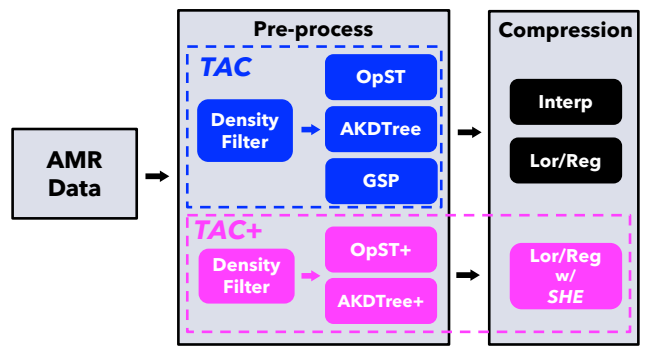


Fig. 3: Workflow overview of our proposed TAC and TAC+.

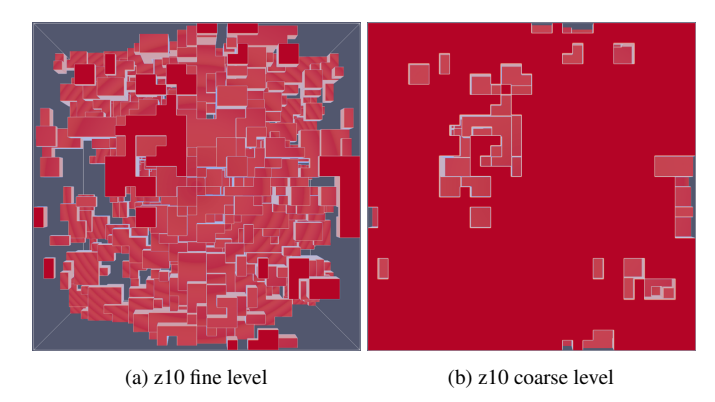


Fig. 4: Visualization of data distributions of an example AMR data "z10", where z = redshift. Non-empty regions are shown in red.

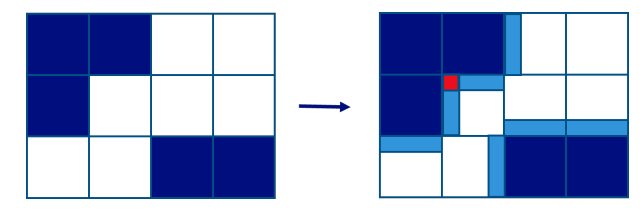


Fig. 5: A 2D example of GSP approach. Non-empty blocks are in navy blue; padded blocks are in light blue/red; padded blocks based on more than one non-empty neighbor are in red.

zeros and pass a large 3D block to the compressor. Although the padded zeros will increase the size of data for compression, for high-density data such as z10's coarse level shown in Figure 4b (i.e., about 77% density), the size overhead will be small.

However, these padded zeros can also greatly reduce the performance of compression, especially for prediction-based lossy compression such as SZ, because these zeros can significantly affect the prediction accuracy of SZ, resulting in high compression errors on the boundaries, as shown in Figure 6a. More specifically, as mentioned in Section III-B, SZ uses each point's neighboring points' values to predict its value. Thus, for those boundary points that are adjacent to padded zeros, SZ will involve zero(s) in the prediction, while the actual values of these empty regions are typically non-zeros (saved in other AMR levels), which will seriously mislead the prediction.

To eliminate the above issue of padding zeroes, we propose to use a ghost-shell padding strategy (**GSP**) to diffuse neighboring values to a padding layer. Figure 5 illustrates the high-level idea, and the detailed algorithm is described in Algorithm 1. Specifically, we first partition the data into unit blocks and then pad each empty unit block by using the average of its non-empty neighbors' boundary data values.

Note that some empty unit blocks have more than one nonempty neighbor such as the red box shown in Figure 5. For these blocks, we will use the average value of all its neighbors for padding. Correspondingly, we will remove these padded values in the decompression based on the saved padding information. Note that since the padding process is only for non-empty blocks, this metadata overhead is almost negligible for highdensity data (e.g., 0.1%).

After padding, each boundary point will be predicted using the average of all the boundary data in the unit block(s) to which it belongs or is neighbored. As shown in Figure 6, compared to the zero-filling (ZF) approach, GSP can significantly reduce the overall compression error, especially for the boundary data.

Algorithm 1: Proposed Ghost Shell Padding Method

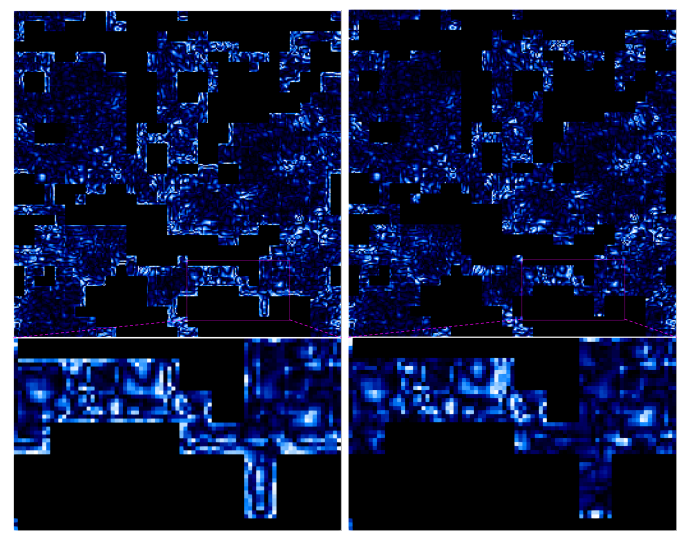
```
Input: Data. m
   Output: Data after padding
1 for each unit block b_i do
       m = min(unitBlockSize/2, 4);
2
3
       if b_i is empty and b_i has non-empty neighbor then
           for each non-empty neighbor n_i do
4
               pad slice = avg (first m slices of n_i next
                to b_i):
               if overlap edge then
                   pad = pad/2;
               else if overlap corner then
                   pad = pad/3;
10
11
                   continue;
12
               end
               add an m-layers pad slice to b_i next to
13
                n_j;
           end
14
15
       end
16 end
17 return padded Data
```

Moreover, the GSP approach can provide a similar compression ratio to the ZF approach on this high-density data and hence a better rate-distortion.

Note that besides using the average values, we can also use values that aid the compression predictor in making the most accurate predictions for padding. However, this requires running the predictor an extra time to determine the best values, making the process more time-consuming. Furthermore, as illustrated in Figure 6, average padding already significantly reduces the compression error on boundary when compared to zero padding. Thus, we chose to use the average values to avoid sacrificing too much performance.

B. Optimized Sparse Tensor Representation for Low-density Data

When most of the regions in the data are empty (e.g., about 77% of the data is empty in Figure 4a), the large amount



(a) ZF (CR=156.7, PSNR=32.8dB) (b) GSP (CR=161.3, PSNR=33.5dB) Fig. 6: Visual comparison (one slice) of compression errors of two approaches using SZ based on Nyx's "baryon density" field (i.e., z10's coarse level, 77% density). Brighter means higher compression error. The error bound is the relative error bound of 6.7×10^{-3} .

of padded data would greatly increase the size of data for compression, resulting in a low compression ratio.

To solve this issue, we propose to use a naive sparse-tensor-based approach (called **NaST**) to remove the empty regions, as shown in Figure 7. NaST includes four main steps in the compression process: (1) partition the 3D data into multiple unit blocks, (2) remove the empty blocks, (3) linearize the remaining 3D blocks into a 4D array, and (4) pass the 4D array to the compressor. Note that in the decompression process, we will put the unit blocks from the decompressed 4D array back into the original data.

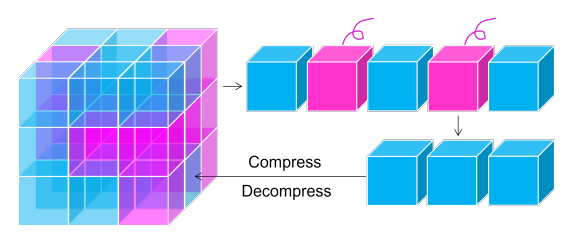


Fig. 7: Workflow of the naive sparse tensor (NaST) method (empty regions marked in pink and non-empty regions marked in blue).

However, in order to completely remove the empty regions to form a sparse representation, the unit block size needs to be relatively small compared to the input data size (e.g., 16^3 vs. 512^3). This results in a reduced spatial locality because of the partitioning. Also, a high proportion of data will be on the block boundary. Given that the linearized unit blocks may not be contiguous in the original dataset, their boundaries aren't smooth, making it challenging for compressors like SZ to predict values accurately." As a result, the NaST method without optimizing the unit block size would have low compression performance.

To address the above problems, we propose an optimized sparse tensor representation (called **OpST**) to effectively remove the empty regions as well as maintain a relatively large unit block size so as to increase the spatial locality and reduce the portion of boundary data. A detailed description of our algorithm can be found in Algorithm 2. We use a 2D example to demonstrate our approach, as illustrated in Figure 8. Specifically, (1) we partition the data into many small unit blocks. (2) For each unit block, we use the dynamic programming method to initiate an array BS to save the dimension/size of the maximum square whose bottom-right corner is that unit block (line 6, which will be discussed in the next paragraph). (3) We extract the sub-blocks (composed of multiple unit blocks) from the original data according to the sizes saved in BS (lines 13). (4) Since the original data will be changed after the extraction, we need to partially update BS based on maxSide (lines 14, will be discussed later). We loop (3) and (4) from the bottom-right corner to the top-left corner until the original data is empty. (5) After extracting all the sub-blocks, we put them into multiple 3D arrays (to be compressed) based on their sizes. Note that the sub-blocks with the same size will be merged into the same array for easy compression.

When initializing the BS in step (2), we start with the b'[i][j] with i=0 or j=0 (i.e., on the top-left edge), where $b'[\cdot][\cdot]$ are the unit blocks: if b'[i][j] is empty, we will set BS[i][j] to 0 otherwise 1. For the remaining unit blocks, if it is empty, BS[i][j] will be 0; otherwise, BS[i][j] will be set to 1 plus the

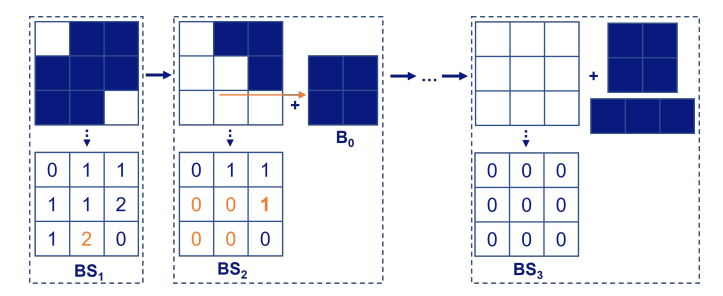
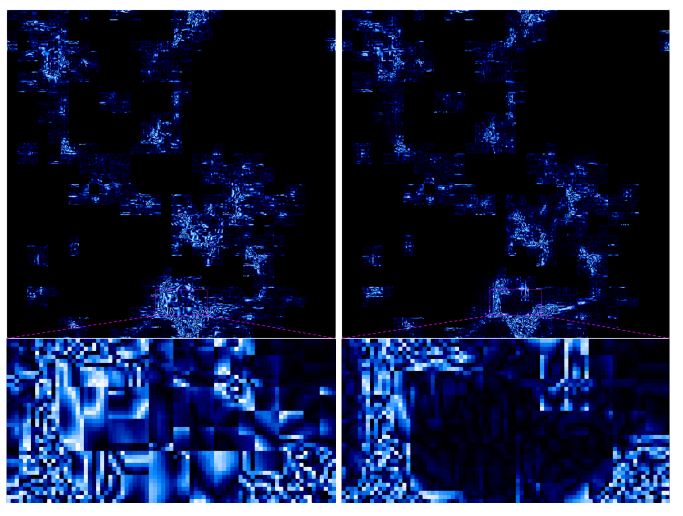


Fig. 8: A 2D example of our proposed OpST approach. The sub-blocks are extracted according to our optimized sizes saved in BS. E.g., a 2-by-2 sub-block B_0 is extracted according to $BS_1[2][1]$.

Algorithm 2: Proposed Optimized Sparse Tensor Method

```
Input: Sparse 3D data S
        Output: multiple 4D array D_n
       for each unit block b(x, y, z) do
                     if b(x, y, z) is non-empty then
 2
  3
                                  if x is 0 or y is 0 or z is 0 then
                                               BS(x, y, z) = 1
                                   else
                                               BS(x, y, z) = \min(BS(x - 1, y, z), BS(x, y - 1, y, z))
                                                   1,z), BS(x,y,z-1), BS(x-1,y-1)
                                                    1, z), BS(x, y - 1, z - 1), BS(x - 1, y, z - 1)
                                                    1), BS(x-1,y-1,z-1))+1;
                                                             BS(x,y,z) is the dimension size of the
                                                    maximum cube whose bottom right rear
                                                    corner is the unit block with index
                                                    (x,y,z) in the original data */
                                               maxSide = max(maxSide, BS(x, y, z))
                                  end
 8
                     end
10 end
11 for each unit block b(x, y, z) do
                     if BS(x, y, z) \ge 1 then
12
                                   size = BS(x, y, z)
13
                                       D_{size} \leftarrow S((x - size : x) * blkSize, (y 
                                      y)*blkSize, (z-size:z)*blkSize); /* put the
                                       sub-block to the according to 4D array */
                                   b(x - size : x, y - size : y, z - size : z) \leftarrow empty
14
                                       BS(x - size : x, y - size : y, z - size : z) = 0
                                       BS = updateBs(BS, x, y, z, maxSide)
                     end
16 end
17 return D_n
```

minimum value among its three neighboring blocks (i.e., upper block, left block, and upper-left block). In other words, we have $BS[i][j] = 1 + \min(BS[i][j-1], BS[i-1][j], BS[i-1][j-1])$ for the 2D case. For example, $BS_1[2][1]$ is 2 because all its upper-left neighbors are 1 (as shown in Figure 8). However, both $BS_1[1][1]$ and $BS_2[1][2]$ can only reach 1 because one of their neighbors is set to 0, having no chance to form a sub-block with the size of 2. Then, for step 3, we perform extraction based on the BS. For instance, as illustrated in Figure 8, according to $BS_1[2][1]$, we extract a 2-by-2 sub-block, B_0 , with its bottom right corner at $BS_1[2][1]$. Moreover, as mentioned in step (4), we need to update BS after each extraction. Specifically, for each sub-block we extract, we have to set its corresponding values in BS to zeros. For instance, as shown in Figure 8, after we extract a 2-by-2 sub-block B_0 at $BS_1[2][1]$, we need to set $BS_2[1][0]$, $BS_2[1][1]$, $BS_2[2][0]$, and $BS_2[2][1]$ to zeros. In addition, we also need to recalculate a part of BS (line 17 in Algorithm 2) because the extraction could influence other BSvalues. For example, we need to recalculate $BS_2[1][2]$ (marked in bold orange) after extracting B_0 . Note that this update is a



(a) NaST(CR=245, PSNR=77.5dB) (b) OpST(CR=248, PSNR=78.0dB) Fig. 9: Visual comparison (one slice) of compression errors of two approaches using SZ based on Nyx's "baryon density" field (i.e., z10's fine level, 23% density). Brighter means higher compression error. The error bound is the relative error bound of 7.2×10^{-4} .

partial update as the BS values to be updated will be bounded by maxSide which is the dimension size of the largest cube in the dataset (line 7).

Similar to NaST, in decompression, we will put the subblocks back to reconstruct the data based on the saved coordinates. Note that after our optimization, each sub-block size will be relatively large (e.g., 96^3 vs the original data size of 512^3), the overhead of saving the coordinates of all the sub-blocks will be negligible (e.g., 0.1%).

Finally, we show a visual comparison of the compression quality between NaST and OpST in Figure 9. Note that both use SZ with the same error bound. Brighter means more errors. We can observe that compared to the NaST method, OpST can significantly reduce the overall compression error, especially for the data points on the boundary. It is worth noting that even with a lower error, our OpST can still provide a higher compression ratio than NaST. This is because our proposed optimization will generate larger sub-blocks, which provide more information for prediction-based lossy compressors such as SZ to achieve better rate-distortion. A detailed evaluation will be shown in Section IV.

C. Adaptive k-D Tree for Medium-density Data

The OpST approach proposed for low-density data, however, has a high computation overhead, especially when the data is relatively dense. This is because, on one hand, OpST needs to update BS based on maxSide for each extraction of a sub-block, while the larger the maxSide, the more values in BS that need to be updated; on the other hand, maxSide is the dimension size of the largest non-empty cube in the dataset, which is highly related to the density of the dataset. Thus, the time complexity of OpST can be expressed as $O(N^2 \cdot d)$, where N is the unit block number and d is the density. Note that here density describes how dense the data is. For example, the density of 77% means that 23% of the data is empty. Clearly, when the density of an AMR level is relatively high, using OpST will be relatively time-consuming.

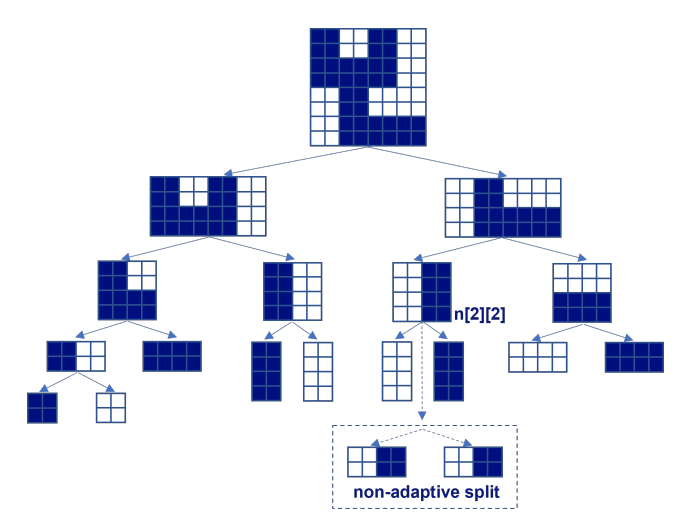


Fig. 10: 2D example of adaptive k-D tree. Sub-block will be adaptively split to effectively remove empty regions and get bigger full sub-blocks.

Algorithm 3: Dynamic k-D Tree

```
Input: data block d, counts information
   Output: k-d tree
2 node.count ← counts information;
3 if d is empty or d is full then
       continue;
                                           /* stop splitting */
5 else
6
       if max(x,y,z)/min(x,y,z) > 2 and pre-split is not over then
           split from the max dimension to get d_1, d_2;
7
           node.left = AKDTree (d_1);
 8
           node.right = AKDTree (d_2);
       else
10
11
           if d is a cube then
               split d equally into 8 oct-blocks:
12
                 s_1,\cdots,s_8;
13
               get the counts c_1,...c_8 for s_1,\cdots,s_8;
               find the maxDiff partition d_1, d_2;
14
               node.left = AKDTree (d_1, four c_i of d_1);
15
16
               node.right = AKDTree (d_2, four c_i of d_2);
17
           else if d is a flat cuboid then
               get the counts c_1,\cdots,c_4 from counts
                 information;
19
               find the maxDiff partition d_1, d_2;
               node.left = AKDTree (d_1, two c_i of d_1);
20
               node.right = AKDTree (d_2, two c_i of d_2);
21
22
           else if d is a slim cuboid then
               get the counts c_1,c_2 from counts
23
                 information;
                \mathsf{split}\ d along the largest dimension to \mathsf{get}
24
                 d_1, d_2;
               node.left = AKDTree (d_1, c_1);
25
               node.right = AKDTree (d_2, c_2);
26
27
       end
28 end
  return node:
```

To address the above high overhead issue of OpST, we propose an adaptive k-d tree, called **AKDTree**, to remove empty regions and extract sub-blocks (containing multiple unit blocks). AKDTree has a lower time complexity of $O(\frac{1}{3}N \cdot \log N)$ (will be discussed later). Figure 10 shows a simple 2D example. Specifically, (1) we partition the data into small unit blocks. (2) We use a tree to hierarchically represent the whole data. Each node in the tree is associated with a sub-block of the data. Moreover, each node stores the number of non-empty unit blocks in the sub-block associated with the node. (3) For each node, we split its associated sub-block from the middle along

one dimension to form two sub-blocks for its two children. Note that while keeping the 3D feature of data, we select one dimension that can maximize the difference of the numbers of non-empty unit blocks of the two children (will be discussed in the next two paragraphs). (4) We keep splitting a node until it has no empty unit block or itself is empty. (5) Once finishing the construction of the tree, we collect all the leaf nodes and send them to the compressor. Note that a non-empty leaf node does not have any empty unit block; otherwise, it will keep splitting. Thus, a leaf node must be an empty or full node, as shown in Figure 10. More detail is described in Algorithm 1.

As mentioned in step (3), We are distributing the non-empty unit blocks unevenly to two children for each node. This is done to maximize the number of leaf nodes with large subblock sizes. Large data blocks contain more spatial information, which can enhance compression. If we keep splitting subblocks in a fixed way, for instance, first split along the x-axis, second split along the y-axis, third split along the x-axis, fourth split along the y-axis, and so on, we will get a 2-by-2 sub-block for the node n[2][2] as shown in the dashed box, while its largest possible sub-block could be 4 by 2 as shown in Figure 10.

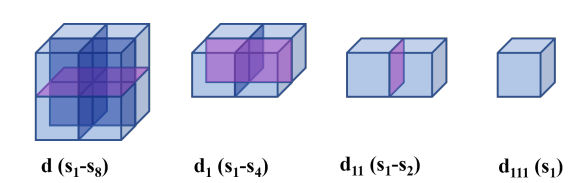


Fig. 11: Example of adaptive splitting, different shapes will have a different number of choices for splitting.

To select one of the dimensions to unevenly distribute its non-empty unit blocks to the two children, we now present our dynamic splitting approach.

To maintain the high-dimensional characteristics of the dataset, it's essential to prioritize splitting along the largest dimension, especially if it is significantly greater than the others. For instance, with a dataset sized $8 \times 8 \times 64$, it's preferable to split along the z-axis rather than the x or y axes. Splitting along the x or y would risk flattening a 3D dataset down to 2D. Consequently, our initial approach is to divide the dataset along the dominant dimension until:

$$max(x, y, z)/min(x, y, z) < 2 \tag{1}$$

Then, we categorize nodes into three different types: "cube" nodes, "flat" nodes, and "slim" nodes, whose dimension ratios are x:y:z, 2x:2y:z (or 2x:y:2z or x:2y:2z), 2x:y:z (or x:y:2z or x:2y:z), respectively. Here, x, y, and z represent the dimensions of the data block after pre-split.

First of all, for the cube node d, we first divide it into eight oct-blocks, i.e., s_1, s_2, \cdots, s_8 (as shown in Figure 11), each sized $\frac{x}{2} \times \frac{y}{2} \times \frac{z}{2}$. x, y, and z are the dimension sizes of the block after pre-split. Then, we can get the counts of non-empty unit blocks of the eight oct-blocks, i.e., c_1, c_2, \cdots, c_8 . After that, we will decide along which dimension to split the cube node d based on the counts. Specifically, we can calculate the following

three differences:

$$\begin{split} & \operatorname{diff}_x = |c_1 + c_3 + c_5 + c_7 - c_2 - c_4 - c_6 - c_8|, \\ & \operatorname{diff}_y = |c_1 + c_2 + c_5 + c_6 - c_3 - c_4 - c_7 - c_8|, \\ & \operatorname{diff}_z = |c_1 + c_2 + c_3 + c_4 - c_5 - c_6 - c_7 - c_8|. \end{split}$$

Finally, we compare these three values and choose the dimension with the maximum difference to split. For example, if the maximum difference is diff_z , we will split d along the z-axis (i.e., the pink 2D plane shown in Figure 11) and get two flat nodes d_1 and d_2 . For the flat nodes such as d_1 , we can reuse c_1 , \cdots , c_4 to decide whether to split d_1 along the x-axis or y-axis by choosing the larger one among the following two differences.

$$\operatorname{diff}_x = |c_1 + c_3 - c_2 - c_4|, \ \operatorname{diff}_y = |c_1 + c_2 - c_3 - c_4|.$$

For the slim nodes such as d_{11} , we simply split it along the x-axis to get two cube nodes s_1 and s_2 . This process (i.e., cube nodes \rightarrow flat nodes \rightarrow slim nodes) in step (3) will be looped until the node becomes a leaf node (empty or full).

Note that based on the above description, the counting process is required for every three nodes in each three paths (i.e., only for the "cube" nodes). Thanks to this dynamic splitting approach, we can lower the time complexity of the AKDTree algorithm to $O(\frac{1}{3} \cdot N \cdot \log N)$, where N is the number of unit blocks while extracting as many relatively large sub-blocks without empty unit block as possible.

In addition, after the dynamic splitting, we will have a series of sub-blocks with the same size but in different directions (e.g., 2x:2y:z, 2x:y:2z, x:2y:2z). We will align the sub-blocks with the same size based on their splitting dimensions (instead of in-memory transposing them), merge them into an array, and compress multiple merged arrays together.

D. Shared Huffman encoding

As mentioned in Section I, III-C, and III-B, the OpST and AKDtree methods collect and linearize the data blocks with the same shape into a 4D array and send it to SZ. However, as highlighted in section III-B, these blocks may not be contiguous in the original dataset. This leads to a lack of locality/smoothness at the boundaries between non-neighbored data blocks, which can still compromise prediction accuracy. This adverse effect is particularly pronounced for SZ's Lor/Reg algorithm. As it is a local prediction algorithm that depends solely on local data, its performance plummets at block boundaries where local smoothness is absent.

A potential solution could be compressing each data block individually using SZ. However, this approach would result in low Huffman encoding efficiency because the entire dataset would be divided into many small blocks, requiring SZ to build a separate Huffman tree for each of these small blocks. In other words, the original SZ method either requires predicting and encoding small blocks together (by forcing them merged into 4D arrays), leading to low prediction accuracy, or predicting and encoding each small block separately, which results in high Huffman encoding overhead. Furthermore, even if the data blocks with the same shape can be compressed together, the data blocks with different shapes still need to be compressed

Algorithm 4: SZ compression with SHE

```
Input: multiple data block D_{1...n}
Output: compressed data S
1 quantCode Q, regreCoeff R, compressed data S;
2 for each data block D_i do
3 | quantCode block q_i, regreCoeff block r_i;
4 | q_i, r_i = SZ.compress(D_i);
5 | Q.append(q_i);
6 | R.append(r_i);
7 end
8 S \leftarrow HuffmanEncode(Q);
9 S \leftarrow HuffmanEncode(R); /* end compression */
10 return S;
```

separately, resulting in low Huffman encoding performance and a high time cost of launching SZ multiple times.

To this end, for OpST and AKDtree, we propose a shared Huffman encoding technique to predict data blocks separately while encoding them together using a single shared Huffman tree. The detail is shown in Algorithm 4. Each data block is first predicted and quantized separately. Then, the quantization codes and regression coefficients of each data block are aggregated to build a shared Huffman tree and encoded at one time. This approach can significantly improve the prediction performance of SZ's Lor/Reg prediction without introducing high time overhead to the encoding of SZ. As shown in Figure 15, compared to the original AKDtree, AKDtree with SHE can significantly reduce the overall compression error, especially for the data located at the boundary of data blocks, leading to significant PSNR improvement, as shown in Figure 16. Furthermore, the use of SHE reduces the number of Huffman trees needed for the data (since we do not need separate Huffman trees for different block shapes), thereby improving encoding efficiency and compression ratio.

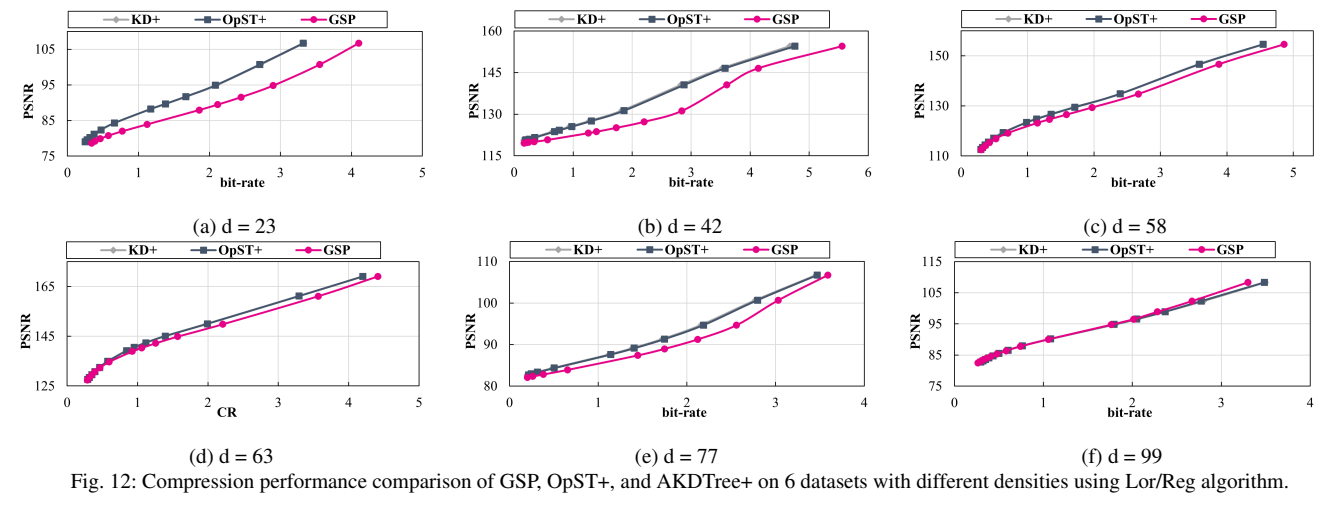
Note that SZ's interpolation does not benefit from SHE. Unlike Lor/Reg that uses only neighboring data for predictions, Interp also considers global points from the dataset. However, with SHE, each small data block produced by OpST or AKDTree is predicted independently. This means Interp loses all global spatial information. In contrast, without SHE, the original OpST and AKDTree methods linearize the data blocks into a large 4D array, preserving more global spatial information for improved prediction. Thus, we exclusively apply the SHE approach to the Lor/Reg predictor.

E. Hybrid Compression Strategy

In this section, we propose a solution to adaptively choose the best-fit compression strategy for both Lor/Reg (with SLE) and Interp algorithms.

For Lor/Reg (with SLE), we will choose from our proposed *OpST with SHE (OpST+)*, *AKDTree with SHE (AKDTree+)*, and *GSP* based on the data characteristics (i.e., data density). According to Section III-B and III-C, OpST+ is more suitable for sparse (i.e., low-density) data, while AKDTree+ is designed to address the high time overhead of OpST+ when the density of data increases. Thus, there should be a data-density threshold to determine when to use OpST+ or AKDTree+.

To decide the threshold T_0 for switching between OpST+ and AKDTree+, we perform a series of experiments using Lor/Reg predictor, as shown in Figure 12. The figure shows that OpST+



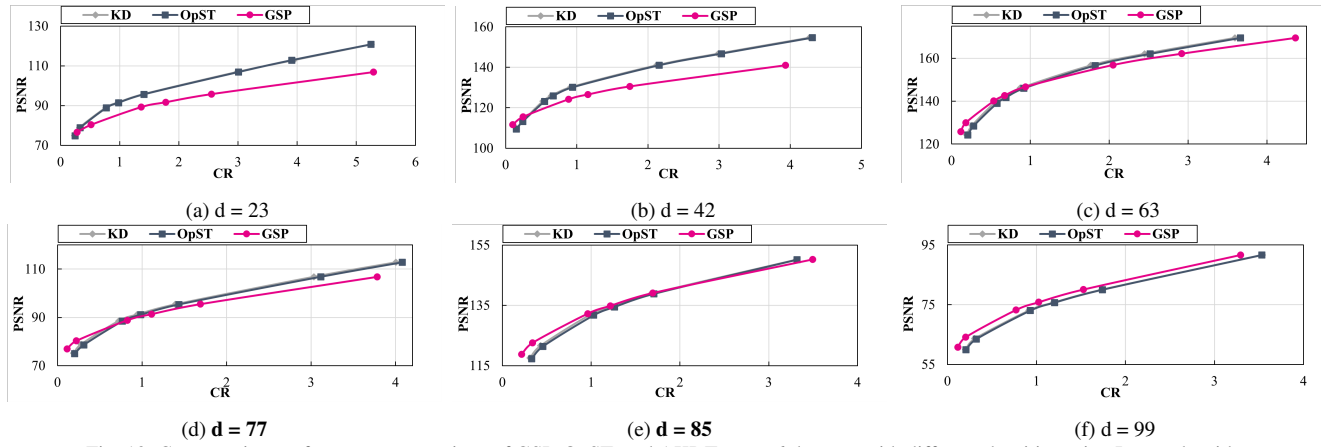


Fig. 13: Compression performance comparison of GSP, OpST, and AKDTree on 6 datasets with different densities using Interp algorithm.

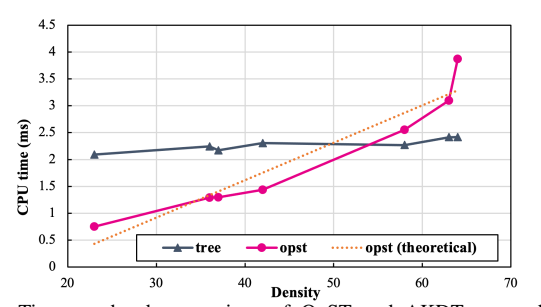
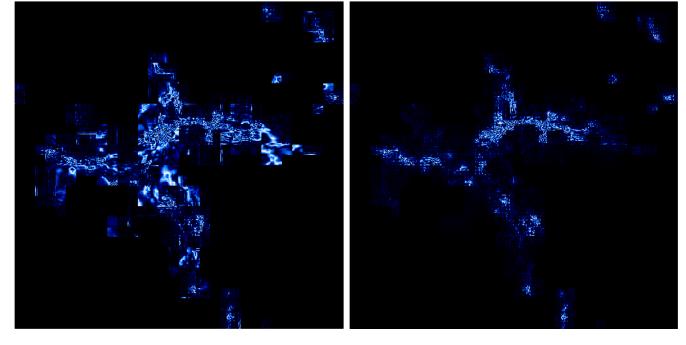


Fig. 14: Time overhead comparison of OpST and AKDTree on different datasets with different densities.

and AKDTree+ have almost identical compression performance in terms of bit-rate and PSNR on all four datasets/levels (from different timesteps) with different densities. Moreover, Figure 14 shows the time costs of OpST+ and AKDTree+ (excluding compression). The figure demonstrates that the time of AKDTree+ is relatively stable, while the time of OpST+ increases linearly with the increase of data density. Overall, the only criterion for selecting OpST+ or AKDTree+ is the time cost rather than the compression performance. This is consistent with our previous design aim, that is, AKDTree is mainly designed to address the high time overhead issue of OpST+. Since OpST+ and AKDTree+ have a similar speed when the density is around 50%, we use T_0 = 50 for choosing OpST+ or AKDTree+.

According to Section III-A, GSP is designed to effectively handle the AMR level with high data density to prevent the



(a) AKDtree (b) AKDtree + SHE (CR=222, PSNR=78.5dB) (CR=231, PSNR=79.6dB)

Fig. 15: Visual comparison (one slice) of compression errors of two approaches using SZ's Lor/Reg prediction on Nyx's "baryon density" field (i.e., z10's fine level, 23% density). Brighter means higher compression error. The error bound is the relative error bound of 4.8×10^{-4} .

negative impact of data partitioning without the use of SHE. In contrast, the data partition methods such as AKDTree require small blocks to be compressed together without SHE, which can significantly decrease prediction accuracy, as shown in Section III-D. However, the negative impact on prediction accuracy caused by the partition can be eliminated by using SHE to compress each small block produced by the partition, which incurs little overhead, while GSP introduces significant overhead to the data size. As shown in Figure 12, OpST+ and AKDTree+ outperform GSP across all the densities. As a result, the improved partition strategies using SHE can be a viable



Fig. 16: Comparison of original AKDTree and AKDTree with SHE on Nyx's "baryon density" field (i.e., z10's fine level, 23% density).

alternative to GSP for all levels.

In summary, for Lor/Reg (with SLE), our proposed hybrid compression approach is described as follows.

- 1) When the density is smaller than $T_0 = 50\%$, we use OpST+ to remove empty regions and then compress;
- 2) When the density is larger than $T_0 = 50\%$, we use AKDTree+ to remove empty regions and then compress.

For the Interp algorithm, we will select from our proposed methods: *OpST*, *AKDTree*, and *GSP*, based on the data density. It is worth noting that we do not employ the SHE approach for the Interp algorithm due to its negligible improvement, as discussed at the end of Section III-D.

To determine the appropriate threshold T_1 for transitioning between OpST and AKDTree, we conducted a series of experiments, as depicted in Figure 13. These figures reveal that both OpST and AKDTree also deliver nearly equivalent compression performance on the Interp algorithm across all six AMR levels, each from different timesteps and with varied densities. Based on these findings, we recommend setting $T_1=50\%$ when selecting between OpST and AKDTree, consistent with our approach for Lor/Reg, aiming to enhance processing speed.

Next, to determine the threshold T_2 for switching between AKDTree and GSP, we also evaluate them on different datasets with different densities. As shown in Figure 13, when the density is relatively low, AKDTree outperforms GSP with respect to both bit-rate and PSNR; when the density gets higher and higher, GSP gradually outperforms AKDTree. We also observe that AKDTree and GSP have similar compression performance when the density is around 85%. Thus, we use $T_2 = 85\%$ to choose AKDTree or GSP.

Therefore, our proposed hybrid compression approach for the Interp algorithm is:

- 1) When the density is smaller than T_1 , we will use OpST to remove empty regions before compression;
- 2) When the density is between T_1 and T_2 , we will use AKDTree to remove empty regions before compression;
- 3) When the density is larger T_2 , we will use GSP to pad appropriate values before compression.

It is evident that, compared to the Lor/Reg with SHE, GSP once again proves beneficial for Interp. The core reason is that, for Lor/Reg, we can use SHE to fully mitigate the impact of partitioning as just mentioned. Interp's global spatial information/locality inevitably gets disrupted by partitioning. GSP can thus be applied to the AMR level with high data density to counteract the effects of partitioning, while also minimizing data size overhead.

F. Discussion on Generality and Distribution

Generality of our design. TAC and TAC+ (including the pre-process strategies and SHE on SZ's Lor/Reg) are designed to handle AMR data level-wise where the data has an irregular distribution, such as many empty/zero regions. TAC/TAC+ can also be employed for sparse non-AMR data compression. However, for sparse non-AMR data with very high density (e.g., 99.9% of the data is non-zero), our TAC/TAC+, designed for irregular data, might not offer many advantages, as this data closely resembles ordinary non-sparse data without empty regions. On the other hand, TAC/TAC+ is more apt for AMR data because AMR data has multi-resolution levels, and the density sum from all levels equals one. This means there is at most one super-dense level where the TAC/TAC+ may be less effective.

Furthermore, the SHE approach can be utilized to enhance the compression ratio while maintaining prediction performance, especially when compressing numerous small-sized datasets collectively. Take, for instance, the scenario of compressing 10,000~2D images of 100×100 . Compressing them individually would result in a reduced overall compression ratio (CR). Conversely, stacking them into a 3D block isn't optimal either, as it could compromise prediction accuracy due to the unsmoothness between images.

Distributed scenario. "In a distributed environment, parallelizing the GSP would be relatively straightforward because its padding approach is primarily local. The only minor challenge arises when padding values must be computed from other processes. This necessitates a boundary value exchange, similar to the Stencil problem.

However, OpST and AKDTree would face more significant challenges in parallelization due to their global nature. Merely using an embarrassingly parallel approach for these algorithms would yield smaller data blocks and lower spatial locality compared to the serial version. It's clear that communication is needed for these algorithms to be more effective, but balancing their ability to extract larger sub-blocks from the dataset with the communication cost would be a challenge. Addressing this challenge will be a primary goal in our future work.

IV. EXPERIMENTAL EVALUATION

A. Experimental Setup

Test data. Our evaluation primarily focuses on the AMReX framework [3], especially the Nyx cosmology simulation [9], the WarpX electromagnetic and electrostatic Particle-In-Cell (PIC) simulation [29], and the IAMR [30], which solves the incompressible Navier-Stokes equation.

Nyx, as shown in Figure 17, is a state-of-the-art, extreme-scale cosmology code that leverages AMReX. It produces six fields, which include baryon density, dark matter density, temperature, and velocities (x, y, and z). We analyzed six datasets produced by three real-world simulation runs, each having different numbers of AMR levels, and simulating a 64 megaparsec (Mpc) region. For these datasets, Z represents the redshift, i.e., the displacement of distant galaxies and celestial objects, as presented in Tab I. Specifically: the first run comprises two levels of refinement, with a coarse level of 256^3

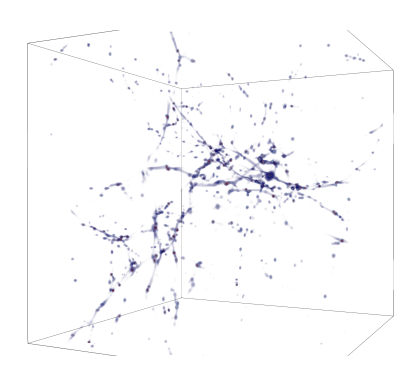


Fig. 17: Visualization of Nyx's density field.

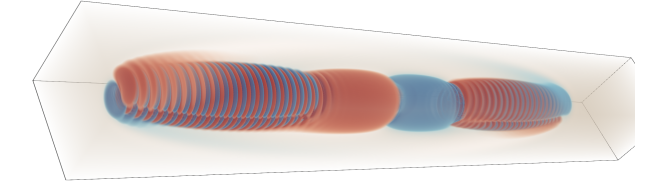


Fig. 18: Visualization of WarpX's electric field (z-direction).

grids and a fine level of 512^3 grids. We collected data from three timesteps, where the finest level density ranges from 23% to 63%. The second run has up to four refinement levels. It began with a resolution of 128^3 and refined to 1024^3 . From this run, we acquired data from two timesteps with the finest-level resolutions of 512^3 (three levels) and 1024^3 (four levels). The density at the finest level ranged from 0.2% to 0.003%. The third run featured three refinement levels with grid sizes of 128^3 at the coarsest level, 256^3 at the intermediate level, and 512^3 at the finest level. The density at the finest level is 0.90%.

WarpX, as shown in Figure 18, is a highly parallel, optimized electromagnetic and electrostatic Particle-In-Cell (PIC) simulation that incorporates AMReX. It is designed to run on GPUs and multi-core CPUs and boasts load-balancing features. WarpX has the capability to scale up to the capacities of the world's most advanced supercomputers. Notably, it was awarded the 2022 ACM Gordon Bell Prize. We collected two timesteps from WarpX, as detailed in Tab I. Each timestep features two refinement levels, with dimensions of $128 \times 128 \times 1024$ and $256 \times 256 \times 2048$. The density at the finest level varies between 2% and 8.6%.

IAMR, as shown in Figure 19, is a highly parallel AMR code to solve the variable-density incompressible Navier-Stokes equations in either 2-D or 3-D. It also offers an embedded boundary (cut cell) representation for intricate geometries. We specifically executed the 3D Rayleigh-Taylor problem, which simulates a heavy fluid atop a light fluid under gravity's influence. We gathered data from two timesteps in IAMR. Each



Fig. 19: Visualization of IAMR's density field.

TABLE I: Our tested AMR applications and datasets.

Dataset	# Levels	Levels Grid Size of Each Level Density of Each Level			
Dataset	# Levels	(Fine to Coarse)	(Fine to Coarse)	(Per timestep)	
Nyx Run1_Z10	2	512, 256	23%, 77%	3.3 GB	
Nyx Run1_Z5	2	512, 256	58%, 42%	6.4 GB	
Nyx Run1_Z2	2	512, 256	63%, 37%	6.7 GB	
Nyx Run2_T3	3	512, 256, 128	0.02%, 0.56%, 99.42%	169 MB	
Nyx Run2_T4	4	1024, 512, 256, 128	3E-5, 0.02%, 2.2%, 97.7%	190 MB	
Nyx Run3_Z1	3	512, 256, 128	0.90%, 14.70%, 84.40%	416 MB	
WarpX_800	2	1282*1024; 2562*2048	8.6%,91.4%	2 GB	
WarpX_1600	2	1282*1024; 2562*2048	2.0%, 98.0%	1.4 GB	
IAMR_90	3	512, 256, 128	0.6%, 10.5%, 88.9%	336 MB	
IAMR_150	3	512, 256, 128	14.8%, 30.9%, 54.3%	2 GB	

timestep comprises three refinement levels, beginning with dimensions of $128 \times 128 \times 128$ for the coarsest level and refining to $512 \times 512 \times 512$ for the finest level. The density at the finest level ranges from 0.6% to 14.8%.

Note that the density of the finest level describes how much of the data in the dataset is at the highest resolution; a higher density of the finest level means that more data is refined to the highest resolution. Usually, the data density is gradually increasing at the finest level, within a single run.

Evaluation platform and compressor. The test platform is equipped with two 28-core Intel Xeon Gold 6238R processors and 384 GB of memory. This work is based on two distinct SZ compression algorithms, namely Lor/Reg, which employs Lorenzo and linear regression predictors, and the Interp, which utilizes the spline interpolation approach as discussed in Section II-A. The Lor/Reg algorithm commences by partitioning the entire input data into $6\times6\times6$ blocks, followed by the independent application of either Lorenzo predictor or high-dimensional linear regression on each individual block. Conversely, the Interp algorithm conducts interpolation across all three dimensions of the entire dataset.

A key distinction between Lor/Reg and Interp is that the former is block-based whereas the latter is global. Specifically, Lor/Reg algorithm divides data into blocks prior to compression, whereas the Interp algorithm applies global interpolation across the entire dataset.

Comparison baselines. As outlined in Section II, we compare against three baselines, either in 1D or 3D, and introduce two of our solutions. Specifically, (1) the 1D baseline (naive): each AMR level is compressed separately as a 1D array; (2) the 1D baseline (zMesh) [28]: we refer readers to Section II for more details about how the zMesh approach reorganize the AMR data for 1D compression; and (3) the 3D baseline: Different AMR levels are unified to the same resolution for 3D compression; (4) our TAC: each AMR level is compressed using OpST (without SHE), AKDTree (without SHE), and GSP based on the data density. For more information, we refer readers to [45] for more details. (5) our TAC+: each AMR level is compressed using OpST+ or AKDTree+ based on the data density, with SHE using Lor/Reg algorithm.

As mentioned in Section III-D, TAC+ is specifically paired with Lor/Reg algorithm. This is because TAC+ is developed to enhance the performance of Lor/Reg compression algorithm using SHE for AMR data. On the other hand, TAC serves as a pre-processing technique, making it compatible with both Lor/Reg and Interp algorithms.

B. Evaluation Metrics

We will evaluate the compression performance based on the following metrics: (1) compression ratio or bit-rate (generic),

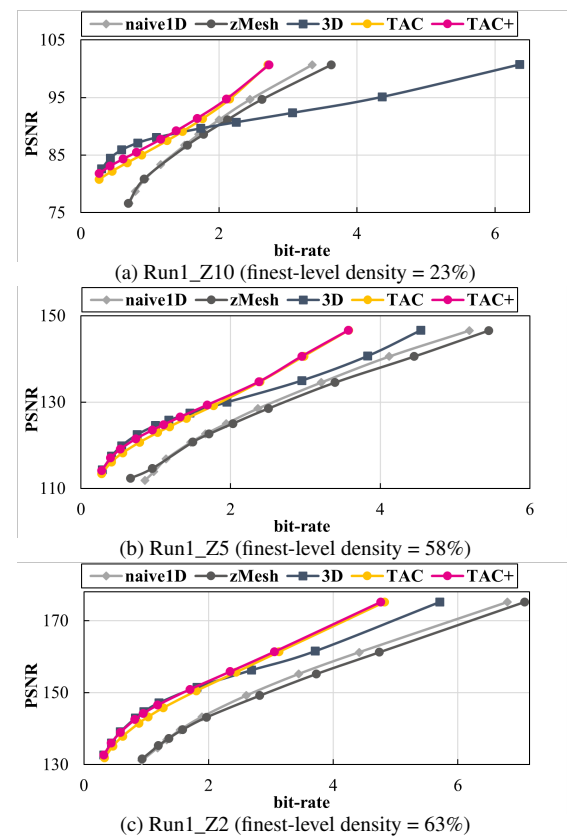


Fig. 20: Rate-distortion comparison of our approaches (TAC and TAC+) and baselines on the early time-step (Z10) to the late time-step (Z2) from Nyx run1 using Lor/Reg algorithm.

(2) distortion quality (generic), (3) compression throughput (generic), (4) rate-distortion (generic), (5) power spectrum (cosmology specific), (6) Halo finder (cosmology specific).

Metric 1: To evaluate the size reduction as a result of the compression, we use the compression ratio, defined as the original data size divided by the compressed data size, or bitrate (bits/value), representing the amortized storage cost of each value. For single/double floating-point data, the bit-rate is 32/64 bits per value before compression. The compression ratio and bit-rate have a mathematical relationship as their multiplication is 32/64 so that a lower bit rate means a higher ratio.

Metric 2: Distortion is another important metric used to evaluate lossy compression quality. We use the peak signal-to-noise ratio (PSNR) to measure the distortion quality.

$$\text{PSNR} = 20 \cdot \log_{10}\left(R_X\right) - 10 \cdot \log_{10}\left(\sum_{i=1}^N e_i^2/N\right),$$

where e_i is the difference between the original and decompressed values for the point i, N is the number of points, and R_X is the value range of X. Higher PSNR means less error.

Metric 3: (De)compression throughputs are critical to improving the I/O performance. We calculate the throughput based on the original data size and (de)compression time.

Metric 4: Similar to prior work [14], [15], [21], [35], [39], [46], [47], we plot the rate-distortion curve to compare the distortion quality with the same bit-rate, for a fair comparison between different compression approaches, taking into account diverse compression algorithms.

Metric 5: Matter distribution in the Universe has evolved to form astrophysical structures on different physical scales, from

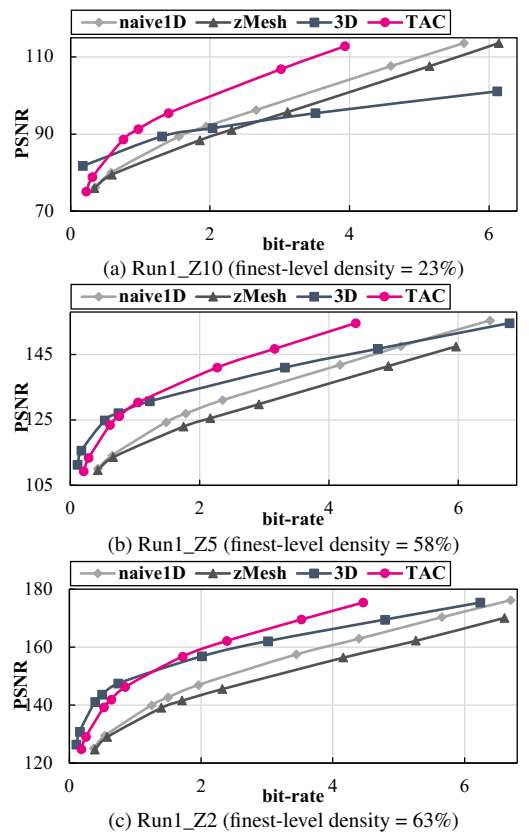


Fig. 21: Rate-distortion comparison of TAC and baselines on the Nyx run1 using Interp algorithm.

planets to larger structures such as superclusters and galaxy filaments. The two-point correlation function $\xi(r)$, which gives the excess probability of finding a galaxy at a certain distance r from another galaxy, statistically describes the amount of the Universe at each physical scale. The Fourier transform of $\xi(r)$ is called the matter power spectrum P(k), where k is the comoving wavenumber. The matter power spectrum describes how much structure exists at each physical scale. We run the power spectrum on the baryon density field by using a cosmology analysis tool called Gimlet. We compare the power spectrum p'(k) of decompressed data with the original p(k) and accept a maximum relative error within 1% for all k < 10.

Metric 6: Halo finder aims to find the halos (over-densities) in the dark matter distribution and output the positions, the number of cells, and the mass for each halo it finds, respectively. Specifically, the halo-finder algorithm [48] searches for the halos from all the simulated data, with the following two criteria: (1) the mass of a data point must be greater than a threshold (e.g., $81.66 \times$ of the average mass of the whole dataset) to become a halo cell candidate [21], [47], [49], and (2) there must be enough halo cell candidates in a certain area to form a halo. For decompressed data, some of the information (mass and cells of halos) can be distorted from the original.

C. Evaluation on Rate-distortion

We first evaluate the rate-distortion of our proposed compression approaches and compare them with the baselines on different simulations and compression algorithms.

For Lor/Reg algorithm, as shown in Figure 20, 22 and 24, our new approach with SHE, TAC+ (represented by the pink

TAC

naive1D ---3D

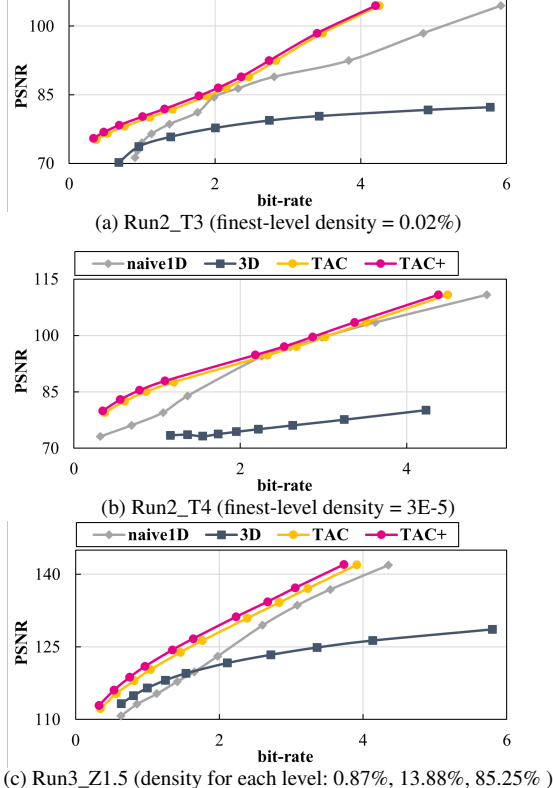


Fig. 22: Rate-distortion comparison of our approaches and baselines on different time-steps from run2 and run3 using Lor/Reg algorithm.

curve) yields better performance than the original TAC (the yellow curve) without SHE for all the datasets from Nyx and IAMR. However, in WarpX, TAC+ does not surpass TAC, as depicted in Figure 26. This can be attributed to the simpler refinement structure of WarpX. Unlike Nyx and IAMR, which refine hundreds of regions (as shown in Figure 4a), WarpX refines only one large rectangular area. Consequently, the unit block size in WarpX is four times larger than in Nyx and IAMR. After the TAC+ partitioning process, this results in a substantially reduced number of unit blocks. This reduction negates the advantages of TAC+, which was specifically developed to handle numerous small AMR data blocks efficiently.

Also, for the 1D baseline, our approaches including the TAC+ and TAC outperform the 1D baseline across all the ten datasets from the three simulations and all two compression algorithms (i.e., Lor/Reg and Interp), as shown in Figure 20 to 27. Furthermore, the performance of our approach is more stable (i.e., smoother curve) than the 1D baseline. We can also find that zMesh is slightly worse than the 1D baseline on our tested data as shown in Figure 20 and 21, which will be explained in the next section.

For the 3D baseline, we observe that our solutions has much better performance when the finest level has a relatively low density or the decompressed data has a high PSNR for all the datasets and compression algorithms, as shown in Figure 20 to 27. However, our approach cannot dominate the 3D baseline as shown in Figure 20 and 21, when the following criteria are satisfied: (1) the AMR data has only two levels of refinement, (2) the finest level has a relatively high density, and (3) the decompressed data has low PSNR/bitrate.

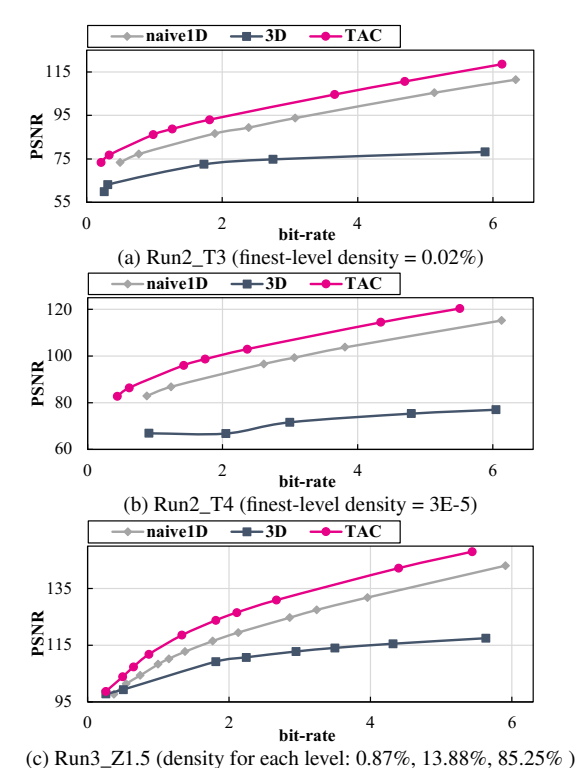


Fig. 23: Rate-distortion comparison of TAC and baselines on Nyx run2 and run3 using Interp algorithm.

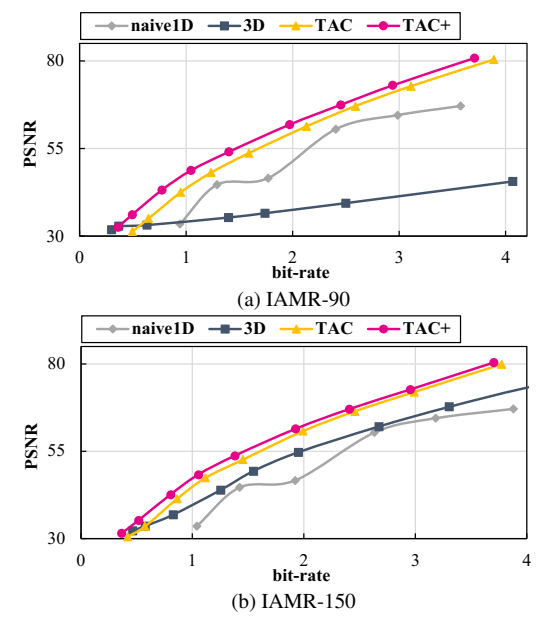


Fig. 24: Rate-distortion comparison of our approaches and baselines on different time-steps from Rayleigh Taylor using Lor/Reg algorithm.

In the next section, we will discuss how the number of AMR levels, the density of the finest level, and the bit-rate/PSNR of decompressed data affect the performance of the 3D baseline and TAC+ and TAC in detail.

D. Comparison with Baselines

On compression, zMesh is meant to improve the smoothness of the patch-based AMR datasets by taking advantage of the data redundancy between each AMR level (as described in the introduction). Thus, zMesh cannot improve the smoothness if there is no data redundancy in the tree-structured AMR datasets (i.e., our tested datasets). A simple example is used to illustrate

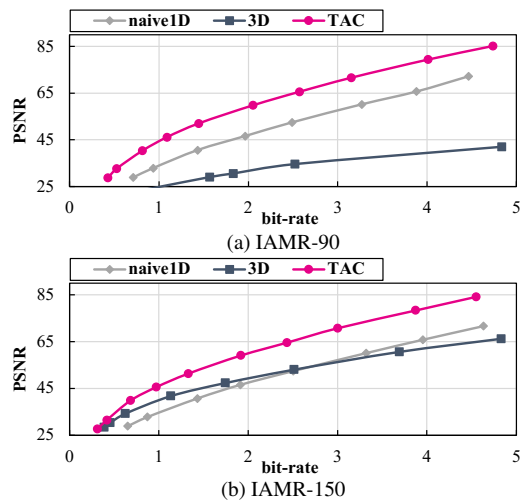


Fig. 25: Rate-distortion comparison of TAC (top-left) and baselines on different time-steps from Rayleigh Taylor using Interp algorithm.

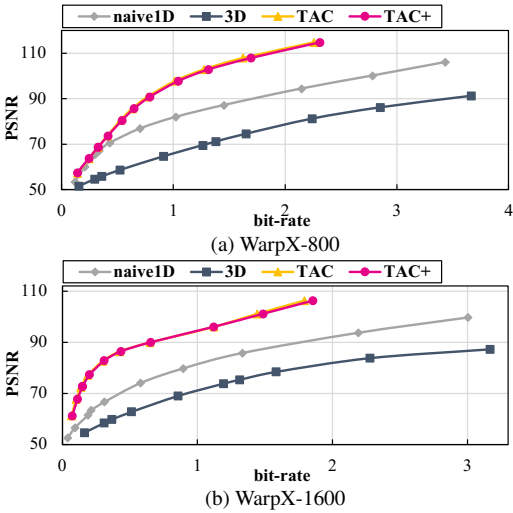


Fig. 26: Rate-distortion comparison of our approaches and baselines on different time-steps from WarpX using Lor/Reg algorithm.

this in Figure 28b, where the finer-level data has higher values because a grid will be refined only if its value is larger than a certain threshold. For block-based AMR, when a grid needs to be refined because of its high value, the value will still remain in the level, resulting in a redundant value saved (i.e., the red 8). If one uses the original z-ordering to traverse the data level-by-level (shown in Figure 28b), the reordered data will have three significant value changes (i.e., from 2 to 8, from 8 to 1, and from 1 to 9). To solve this issue, zMesh traverses the two AMR levels together based on the layout of the 2D array. The reordered data are "1-2-8-9-8-7-8-1", which only has two significant value changes (from 2 to 8 and from 8 to 1). Thus, zMesh can improve the smoothness of patch-based AMR data.

However, as shown in Figure 28a, for tree-structured AMR data (without saving a redundant "8"), compared to the 1D baseline that compresses each level separately, zMesh introduces two significant data changes (i.e., from 2 to 9 and from 8 to 1) as it traverses between two AMR levels. This explains why zMesh is slightly worse than the 1D baseline.

When considering the 3D baseline, we observe that it works slightly better than TAC+ in the following circumstances: (1) the AMR data has only two levels of refinement, (2) the finest

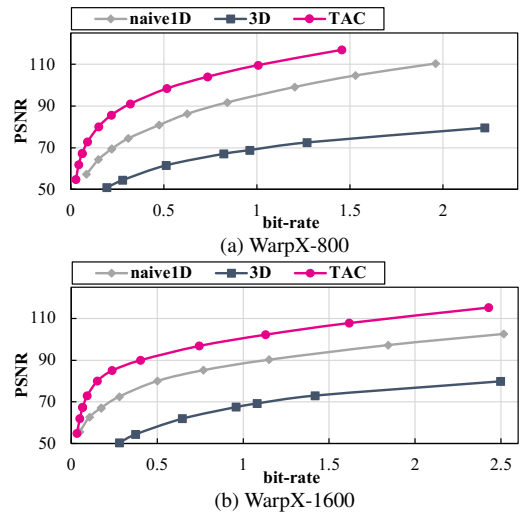
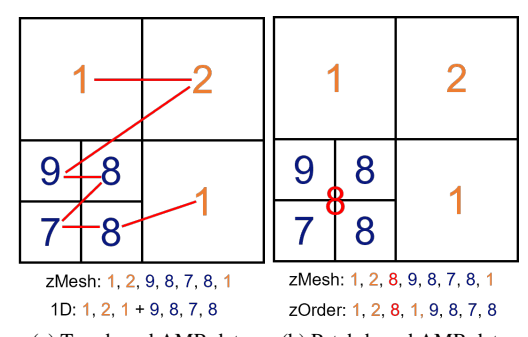


Fig. 27: Rate-distortion comparison of TAC+ and baselines on different timesteps from WarpX using Interp algorithm.



(a) Tree-based AMR data
(b) Patch-based AMR data
Fig. 28: An example of how the 1D baseline, zMesh, and original z-order
reorder a simple 2D AMR data without and with redundancy. Orange: coarse
level, blue: fine level, red: redundant data.

level of the data has a relatively high density, and (3) the decompressed data has a low PSNR/bit-rate.

We now explain each observation point individually. As outlined in Section II-D, a primary drawback of the 3D baseline is the redundant data produced by the up-sampling process. This redundancy becomes even more pronounced for AMR data with more than two refinement levels, especially when the finest level of data is sparsely populated. Such extra data increases the data size, leading to sub-optimal compression performance for the 3D baseline (points 1 & 2).

Conversely, the 3D baseline yields superior data locality and smoothness compared to TAC+ and TAC. This is because it processes the entire dataset as a unified block, without segmenting it. Consequently, the 3D baseline exhibits enhanced compressibility, resulting in a quicker bitrate reduction and a slower reduction in PSNR as the error bound increases, compared to TAC+ and TAC. As a result, the 3D baseline performs better at a low bit-rate (point 3).

E. TAC/TAC+ for Different Compression Algorithms

Note that the Lor/Reg compression algorithm can use the enhanced TAC+, resulting in improved compression performance. Conversely, with the Interp, we did not use TAC+ because it cannot bring a performance advantage over TAC as mentioned in Section III-D. The underlying reason for this difference lies in the nature of the AMR data and the

Lor/Reg algorithm. Both AMR data and Lor/Reg are block-based, whereas Interp is global.

Specifically, a significant challenge in compressing highdimensional AMR data is the need for partitioning, which can compromise spatial information and data smoothness. Given that Lor/Reg also segments data into blocks, it aligns naturally with the partitioning approach inherent to AMR data. By leveraging our pre-process and optimization technique, Lor/Reg combined with TAC+ using SLE can effectively address the issues of local data smoothness and smoothness caused by partitioning, making it especially compatible with AMR data. In contrast, the Interp method implements a global interpolation approach on partitioned AMR data. Due to partitioning, small-sized blocks inevitably disrupt global spatial information for global interpolation. Although we can use the OpST and AKDTree to obtain larger partitioned blocks and improve spatial locality, we still cannot achieve perfect compatibility between interpolation prediction and AMR data.

F. Post-analysis Quality with Adaptive Error Bound

TABLE II: Halo finder analysis with different methods.

	CR	Avg Rel Mass Diff	Avg Rel Cells Diff
3D baseline	188.7	2.7E-04	2.2E-03
TAC+ (1:1)	189.1	2.2E-04	2.1E-03
TAC+ (2:1)	192.5	1.1E-04	9.0E-04

When factoring level-wise compression, our approach can apply different error bounds to different AMR levels based on (1) the post-analysis metrics, (2) the up-sampling rates of coarse levels, and (3) the rate-distortion trade-off between different AMR levels. We now evaluate our approach with the two cosmology-specific post-analysis metrics (i.e., power spectrum and halo finder) to demonstrate the benefit of the adaptive error bound method. We chose the dataset run1-Z2 for evaluation because TAC+ has a similar performance as the 3D baseline on this dataset.

Figure 29 shows the motivation of performing rate-distortion trade-off between different AMR levels. As the error bounds for the fine and coarse levels increase, their bit rates will converge to a similar value. This means that when the error bound is relatively large, the reduction in data size will be insignificant compared to the compression error increment (i.e., the slopes of both curves are small). Thus, we conclude that when the error is large, trading data quality for size reduction is not worth.

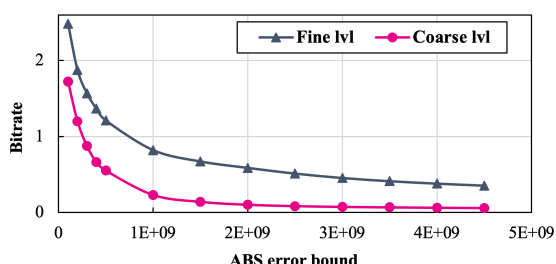


Fig. 29: Bit-rates with different error bounds using SZ lossy compression for fine and coarse levels on Run1_Z2 dataset.

Power Spectrum Figure 30a shows that under the (almost) same compression ratio, TAC+ (with the uniform error bound) has a better power-spectrum error compared to the 3D baseline.

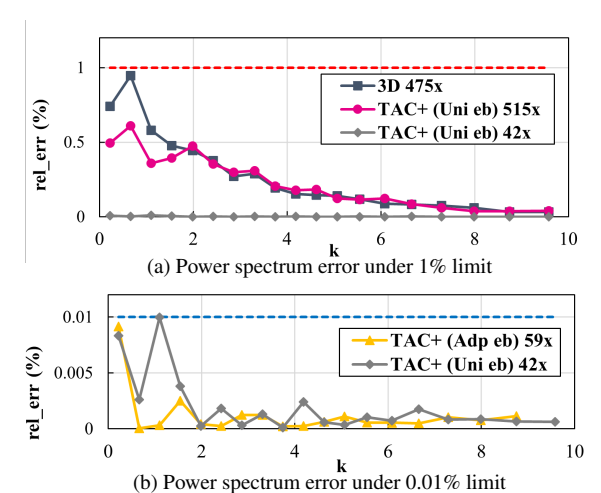


Fig. 30: Power spectrum error (in relative) of the 3D baseline and TAC+ (uniform error bound) and TAC+ (adaptive error bound) on baryon density field on run1-Z2. The red and blue dashed line is the 1% and 0.01% limit of acceptable power spectrum error.

Also note that TAC+ yields nearly lossless power-spectrum distortion (less than 0.01%) under the compression ratio of $42\times$, as shown in Figure 30a's gray curve.

Now, let us follow the three steps mentioned at the beginning of this section to adjust the error bound for each AMR level. First, the post-analysis metric–power spectrum—needs to be run on the uniform-resolution data and focuses on the global quality of data. Thus, the ideal error-bound configuration/ratio for the fine and coarse levels on the uniform-resolution data would be 1:1.

as mentioned before, the coarse level of the AMR dataset needs to be up-sampled to uniform the resolution. As a result, the compression error of the coarse level will be up-sampled as well, resulting in more error in the post-analysis. Thus, we then need to give the coarse level a smaller error bound based on the up-sample rate. Here the up-sample rate for Z2's coarse level is 2^3 , leading to an ideal error-bound ratio of the fine and coarse levels changed to 8:1.

Finally, this 8:1 ratio needs to be adjusted based on the rate-distortion trade-off as mentioned before. As shown in Figure 29, when using the error-bound ratio of 8:1 (e.g., 4E+9 for the fine level and 5E+8 for the coarse level), the error bound of the fine level is too large, resulting in an ineffective rate-distortion trade-off. Thus, we can balance two levels by increasing the error bound for the coarse level (to gain compression ratio) and decreasing the error bound for the fine level (to add compression error), which can achieve an overall rate-distortion benefit. Based on our experiments, we adjust the error-bound ratio from 8:1 to 3:1, As shown in Figure 30b, TAC+ with adaptive error bound can significantly improve the compression ratio compared with uniform error bound under similar power spectrum error.

Halo finer We evaluate the mass change, and the number of cells change for the three largest halos identified using the 3D baseline, TAC+ (with uniform error bound), and TAC+ (with adaptive error bound), as shown in Table II. We can see that TAC+ with uniform error bound produces better halo-finer analysis quality than the 3D baseline.

Similar to the error-bound configuration analysis done for

TABLE III: Overall compression/decompression throughputs (MB/s) of different approaches with different absolute error bounds on Nyx.

Comp	EB_abs		Ru	n1_Z10		Run1_Z2			Run2_T4				Run3_Z1				
Algo	EB_aus	1D	3D	TAC	TAC+	1D	3D	TAC	TAC+	1D	3D	TAC	TAC+	1D	3D	TAC	TAC+
	1E+08	51	37	79	77	51	79	85	84	49	0.32	24	24	49	5.6	63	63
Lor/Reg	1E+09	81	48	94	93	55	92	103	97	53	0.39	26	26	53	6.5	78	75
	1E+10	89	53	107	102	58	100	111	104	84	0.41	28	27	57	7.1	91	84
	1E+08	74	35	80	\	73	73	90	\	67	0.27	24	\	68	4.9	70	\
Interp	1E+09	82	42	91	\	82	81	95	\	77	0.32	25	١	78	5.8	77	\
	1E+10	90	46	97	١	87	85	104	\	84	0.33	26	\	87	6.3	87	\

TABLE IV: Overall compression/decompression throughputs (MB/s) of different approaches with different absolute error bounds on IAMR.

Comp	EB_abs		IA	IAMR_90 IAMR_150					
Algo	LD_aos	1D	3D	TAC	TAC+	1D	3D	TAC	TAC+
Lor/Reg	2E+03	50	5.0	67	66	51	28	76	78
	2E+04	52	5.2	73	71	50	30	85	86
	2E+05	54	5.6	79	78	53	31	94	94
Interp	2E+03	72	4.6	68	\	68	25	81	\
	2E+04	80	4.8	75	\	78	27	92	\
	2E+05	86	5.1	80	\	81	28	96	\

TABLE V: Overall compression/decompression throughput (MB/s) of different approaches with different absolute error bounds on WarpX.

Comp	EB_abs		Wai	pX_800)	WarpX_1600				
Algo	ED_aus	1D	3D	TAC	TAC+	1D	3D	TAC	TAC+	
Lor/Reg	1E+06	49	15	97	85	47	8.9	102	89	
	1E+07	52	18	107	92	50	11	126	103	
	1E+08	52	19	115	98	53	14	159	121	
Interp	1E+06	73	14	128	\	68	8.7	123	\	
	1E+07	79	16	140	\	75	11	140	\	
	1E+08	83	17	147	١	79	12	159	/	

the power spectrum, let us now adjust the error-bound ratio between the fine and coarse levels for halo finder. The halofiner analysis also requires uniform-resolution data as input. However, different from the power-spectrum analysis, the halofinder analysis focuses more on high-value points at the fine level, since only high-value data points qualify as halo candidates, as described in Section IV-B. Note that this does not mean we can directly discard the coarse-level data with small values as they still contribute to the average value of the dataset, which is also an important parameter for the halo finder [48]. Therefore, we set the ideal error-bound ratio to 1:2 (i.e., fine level vs coarse level) for the uniform-resolution data based on our massive experiments. After that, considering the upsampling rate of 2^3 , the error-bounded ratio is changed to 4:1. Finally, we adjust the ratio to 2:1 based on the rate-distortion trade-off. Table II shows that TAC+ with adaptive error bound obtains the minimal differences of the mass and cell numbers.

G. Evaluation on Time Overhead

We evaluate the overall throughput (including pre-process and (de)compression) on the datasets with different error bounds. As shown in Table III, IV, and V, compared to the 3D baseline, the throughput of TAC+ is up to $2 \times$ higher on the Nyx Run1 datasets, 75× higher on the Nyx Run2 dataset, 11.8× higher on the Nyx Run1 dataset, 10× higher on IAMR dataset, and 14× higher on WarpX dataset. This is because the WarpX, IAMR, Nyx Run2, and Nyx Run3 datasets have a lower density than the Run1 datasets at the finest level, resulting in a higher overhead of redundant data for the 3D baseline, which is consistent with our discussion in Section IV-D. We note that TAC+ and performs better than the 1D baseline on all the tested datasets except the Nyx Run2_T4 datasets, due to its long data-partition time (relative to the total time) on the smallsized datasets. Also, in the three tables, the symbol "\" denotes that TAC+ is specifically paired with the Lor/Reg algorithm as mentioned in Section IV-A.

The overall higher throughput of both TAC+ and TAC can be attributed to the high efficiency of the three pre-process strategies. Firstly, the GSP pre-process operates in linear time, as only a subset of the boundary data needs to be processed once to calculate the padding value. Additionally, padding is restricted to specific empty regions and is executed just once. Next, the time complexities for $\operatorname{OpSt}(+)$ and $\operatorname{AKDTree}(+)$ are $O(N^2 \cdot d)$ and $O(\frac{1}{3}N \cdot \log N)$ respectively, where N represent the unit block number and d indicates the density. Given that each unit block comprises a substantial number of data points, both $\operatorname{OpSt}(+)$ and $\operatorname{AKDTree}(+)$ exhibit high efficiency. Moreover, by employing our hybrid compression strategy detailed in Section III-E, we can further enhance the performance of $\operatorname{TAC}(+)$ by opting for the faster algorithm between $\operatorname{OpSt}(+)$ and $\operatorname{AKDTree}(+)$.

In addition, TAC+ has almost the same throughput as TAC. The very slight decrease is because TAC+ compresses the data in a more fine-grained manner. We exclude zMesh in this evaluation as it is theoretically slower than the 1D baseline due to the extra z-ordering and provides worse rate-distortion according to our evaluation.

V. CONCLUSION AND FUTURE WORK

In conclusion, this paper leverages 3D compression for AMR data on a systemic level. We propose three pre-process strategies that can adapt based on the density of each AMR level. Our approach improves the compression ratio compared to the state-of-the-art approach by up to $4.9\times$ under the same data quality loss. With our level-wised compression approach, we are able to tune the error-bound ratio of fine and coarse levels to be 3:1 and 2:1 for better power-spectrum and halo-finder analyses, respectively, under the same compression ratio. In future work, we will apply TAC+ to more AMR simulations and improve its throughput on multi-core CPUs using OpenMP and GPUs using CUDA.

ACKNOWLEDGEMENT

This work has been authored by employees of Triad National Security, LLC, which operates Los Alamos National Laboratory under Contract No. 89233218CNA000001 with the U.S. Department of Energy (DOE) and the National Nuclear Security Administration (NNSA). This research was supported by the Exascale Computing Project (ECP), Project Number: 17-SC-20-SC, a collaborative effort of the DOE SC and NNSA. This work was also supported by NSF awards 2303064, 2247080, 2311876, and 2312673. This research used resources of the National Energy Research Scientific Computing Center, a DOE SC User Facility located at Lawrence Berkeley National Laboratory, operated under Contract No. DE-AC02-05CH11231. We would like to thank Dr. Zarija Lukić and Dr. Jean Sexton from the NYX team at Lawrence Berkeley National Laboratory for granting us access to cosmology datasets. This research used the open-source particlein-cell code WarpX, primarily funded by the US DOE Exascale Computing Project.

REFERENCES

- C. Burstedde, O. Ghattas, G. Stadler, T. Tu, and L. C. Wilcox, "Towards adaptive mesh pde simulations on petascale computers," *Proceedings of Teragrid*, vol. 8, 2008.
- [2] A. Dubey, A. Almgren, J. Bell, M. Berzins, S. Brandt, G. Bryan, P. Colella, D. Graves, M. Lijewski, F. Löffler et al., "A survey of high level frameworks in block-structured adaptive mesh refinement packages," *Journal of Parallel and Distributed Computing*, vol. 74, no. 12, pp. 3217– 3227, 2014.
- [3] W. Zhang, A. Almgren, V. Beckner, J. Bell, J. Blaschke, C. Chan, M. Day, B. Friesen, K. Gott, D. Graves *et al.*, "Amrex: a framework for blockstructured adaptive mesh refinement," *Journal of Open Source Software*, vol. 4, no. 37, pp. 1370–1370, 2019.
- [4] J. M. Stone, K. Tomida, C. J. White, and K. G. Felker, "The athena++ adaptive mesh refinement framework: Design and magnetohydrodynamic solvers," *The Astrophysical Journal Supplement Series*, vol. 249, no. 1, p. 4, 2020.
- [5] A. S. Almgren, J. B. Bell, M. J. Lijewski, Z. Lukić, and E. Van Andel, "Nyx: A massively parallel amr code for computational cosmology," *The Astrophysical Journal*, vol. 765, no. 1, p. 39, 2013.
- [6] B. Runnels, V. Agrawal, W. Zhang, and A. Almgren, "Massively parallel finite difference elasticity using block-structured adaptive mesh refinement with a geometric multigrid solver," *Journal of Computational Physics*, vol. 427, p. 110065, 2021.
- [7] S. Whitman, J. Brasseur, and P. Hamlington, "Simulation of bluff-body stabilized flames with pelec, an exascale combustion code," 2018.
- [8] K. Sverdrup, N. Nikiforakis, and A. Almgren, "Highly parallelisable simulations of time-dependent viscoplastic fluid flow with structured adaptive mesh refinement," *Physics of Fluids*, vol. 30, no. 9, p. 093102, 2018.
- [9] Nyx, https://github.com/AMReX-Astro/Nyx, 2021.
- [10] P. Deutsch, "Gzip file format specification version 4.3," 1996.
- [11] Zstandard, http://facebook.github.io/zstd/, 2020.
- [12] S. W. Son, Z. Chen, W. Hendrix, A. Agrawal, W.-k. Liao, and A. Choud-hary, "Data compression for the exascale computing era-survey," *Super-computing Frontiers and Innovations*, vol. 1, no. 2, pp. 76–88, 2014.
- [13] S. Di and F. Cappello, "Fast error-bounded lossy hpc data compression with sz," in 2016 ieee international parallel and distributed processing symposium (ipdps). IEEE, 2016, pp. 730–739.
- [14] D. Tao, S. Di, Z. Chen, and F. Cappello, "Significantly improving lossy compression for scientific data sets based on multidimensional prediction and error-controlled quantization," in 2017 IEEE International Parallel and Distributed Processing Symposium (IPDPS). IEEE, 2017, pp. 1129– 1139.
- [15] X. Liang, S. Di, D. Tao, S. Li, S. Li, H. Guo, Z. Chen, and F. Cappello, "Error-controlled lossy compression optimized for high compression ratios of scientific datasets," in 2018 IEEE International Conference on Big Data. IEEE, 2018.
- [16] P. Lindstrom, "Fixed-rate compressed floating-point arrays," *IEEE Transactions on Visualization and Computer Graphics*, vol. 20, no. 12, pp. 2674–2683, 2014.
- [17] M. Ainsworth, O. Tugluk, B. Whitney, and S. Klasky, "Mgard: A multilevel technique for compression of floating-point data," in *DRBSD-2 Workshop at Supercomputing*, 2017.
- [18] X. Liang, B. Whitney, J. Chen, L. Wan, Q. Liu, D. Tao, J. Kress, D. Pugmire, M. Wolf, N. Podhorszki et al., "Mgard+: Optimizing multilevel methods for error-bounded scientific data reduction," *IEEE Transactions on Computers*, vol. 71, no. 7, pp. 1522–1536, 2021.
- [19] R. Ballester-Ripoll, P. Lindstrom, and R. Pajarola, "Tthresh: Tensor compression for multidimensional visual data," *IEEE Transactions on Visualization and Computer Graphics*, vol. 26, no. 9, pp. 2891–2903, 2020.
- [20] F. Cappello, S. Di, S. Li, X. Liang, A. M. Gok, D. Tao, C. H. Yoon, X.-C. Wu, Y. Alexeev, and F. T. Chong, "Use cases of lossy compression for floating-point data in scientific data sets," *The International Journal of High Performance Computing Applications*, 2019.
- [21] S. Jin, P. Grosset, C. M. Biwer, J. Pulido, J. Tian, D. Tao, and J. Ahrens, "Understanding gpu-based lossy compression for extreme-scale cosmological simulations," in 2020 IEEE International Parallel and Distributed Processing Symposium (IPDPS). IEEE, 2020, pp. 105–115.
- [22] P. Grosset, C. M. Biwer, J. Pulido, A. T. Mohan, A. Biswas, J. Patchett, T. L. Turton, D. H. Rogers, D. Livescu, and J. Ahrens, "Foresight: analysis that matters for data reduction," in SC20: International Conference for High Performance Computing, Networking, Storage and Analysis. IEEE, 2020, pp. 1–15.

- [23] T. Lu, Q. Liu, X. He, H. Luo, E. Suchyta, J. Choi, N. Podhorszki, S. Klasky, M. Wolf, T. Liu et al., "Understanding and modeling lossy compression schemes on hpc scientific data," in 2018 IEEE International Parallel and Distributed Processing Symposium (IPDPS). IEEE, 2018, pp. 348–357.
- [24] A. H. Baker, H. Xu, J. M. Dennis, M. N. Levy, D. Nychka, S. A. Mickelson, J. Edwards, M. Vertenstein, and A. Wegener, "A methodology for evaluating the impact of data compression on climate simulation data," in *Proceedings of the 23rd International Symposium on High-Performance Parallel and Distributed Computing*. ACM, 2014, pp. 203–214.
- [25] A. H. Baker, H. Xu, D. M. Hammerling, S. Li, and J. P. Clyne, "Toward a multi-method approach: Lossy data compression for climate simulation data," in *International Conference on High Performance Computing*. Springer, 2017, pp. 30–42.
- [26] A. M. Gok, S. Di, Y. Alexeev, D. Tao, V. Mironov, X. Liang, and F. Cappello, "Pastri: Error-bounded lossy compression for two-electron integrals in quantum chemistry," in 2018 IEEE international conference on cluster computing (CLUSTER). IEEE, 2018, pp. 1–11.
- [27] X.-C. Wu, S. Di, E. M. Dasgupta, F. Cappello, H. Finkel, Y. Alexeev, and F. T. Chong, "Full-state quantum circuit simulation by using data compression," in *Proceedings of the International Conference for High Performance Computing, Networking, Storage and Analysis*, 2019, pp. 1–24.
- [28] H. Luo, J. Wang, Q. Liu, J. Chen, S. Klasky, and N. Podhorszki, "zmesh: Exploring application characteristics to improve lossy compression ratio for adaptive mesh refinement," in 2021 IEEE International Parallel and Distributed Processing Symposium (IPDPS). IEEE, 2021, pp. 402–411.
- [29] L. Fedeli, A. Huebl, F. Boillod-Cerneux, T. Clark, K. Gott, C. Hillairet, S. Jaure, A. Leblanc, R. Lehe, A. Myers et al., "Pushing the frontier in the design of laser-based electron accelerators with groundbreaking mesh-refined particle-in-cell simulations on exascale-class supercomputers," in SC22: international conference for high performance computing, networking, storage and analysis. IEEE, 2022, pp. 1–12.
- [30] IAMR, https://github.com/AMReX-Codes/IAMR, 2023.
- [31] S. Jin, S. Di, F. Vivien, D. Wang, Y. Robert, D. Tao, and F. Cappello, "Concealing compression-accelerated i/o for hpc applications through in situ task scheduling," in *EuroSys* 2024, 2024.
- [32] G. K. Wallace, "The JPEG still picture compression standard," *IEEE Transactions on Consumer Electronics*, vol. 38, no. 1, pp. xviii–xxxiv, 1992.
- [33] D. Le Gall, "Mpeg: A video compression standard for multimedia applications," *Communications of the ACM*, vol. 34, no. 4, pp. 46–58, 1991.
- [34] K. Zhao, S. Di, M. Dmitriev, T.-L. D. Tonellot, Z. Chen, and F. Cappello, "Optimizing error-bounded lossy compression for scientific data by dynamic spline interpolation," in 2021 IEEE 37th International Conference on Data Engineering. IEEE, 2021, pp. 1643–1654.
- [35] X. Liang, Q. Gong, J. Chen, B. Whitney, L. Wan, Q. Liu, D. Pugmire, R. Archibald, N. Podhorszki, and S. Klasky, "Error-controlled, progressive, and adaptable retrieval of scientific data with multilevel decomposition," in *Proceedings of the International Conference for High Performance Computing, Networking, Storage and Analysis*, 2021, pp. 1–13
- [36] F. Wang, N. Marshak, W. Usher, C. Burstedde, A. Knoll, T. Heister, and C. Johnson, "Cpu ray tracing of tree-based adaptive mesh refinement data," *Computer Graphics Forum*, vol. 39, pp. 1–12, 06 2020.
- [37] G. Harel, J.-B. Lekien, and P. Pébaÿ, "Two new contributions to the visualization of amr grids: I. interactive rendering of extreme-scale 2dimensional grids ii. novel selection filters in arbitrary dimension," 03 2017.
- [38] D. Wang, J. Pulido, P. Grosset, J. Tian, J. Ahrens, and D. Tao, "Analyzing impact of data reduction techniques on visualization for amr applications using amrex framework," in *Proceedings of the SC'23 Workshops of The International Conference on High Performance Computing, Network, Storage, and Analysis*, 2023, pp. 263–271.
- [39] K. Zhao, S. Di, X. Liang, S. Li, D. Tao, Z. Chen, and F. Cappello, "Significantly improving lossy compression for hpc datasets with secondorder prediction and parameter optimization," in *Proceedings of the 29th International Symposium on High-Performance Parallel and Distributed Computing*, 2020, pp. 89–100.
- [40] D. Wang, J. Pulido, P. Grosset, J. Tian, S. Jin, H. Tang, J. Sexton, S. Di, K. Zhao, B. Fang et al., "Amric: A novel in situ lossy compression framework for efficient i/o in adaptive mesh refinement applications," in Proceedings of the International Conference for High Performance Computing, Networking, Storage and Analysis, 2023, pp. 1–15.

- [41] J. Bentley, "Multidimensional binary search trees used for associative searching," communications of the ACM September, 1975. vol. 18: pp. 509-517: ill. includes bibliography., vol. 18, 01 1975.
- [42] D. Hoang, H. Bhatia, P. Lindstrom, and V. Pascucci, "High-quality and low-memory-footprint progressive decoding of large-scale particle data," in 2021 IEEE 11th Symposium on Large Data Analysis and Visualization (LDAV). IEEE Computer Society, 2021, pp. 32–42.
- [43] G. Cirio, G. Lavoué, and F. Dupont, "A framework for data-driven progressive mesh compression." in *GRAPP*, 2010, pp. 5–12.
- [44] O. Devillers and P.-M. Gandoin, "Geometric compression for interactive transmission," *Proc. Visualization* '00, 01 2000.
- [45] D. Wang, J. Pulido, P. Grosset, S. Jin, J. Tian, J. Ahrens, and D. Tao, "Tac: Optimizing error-bounded lossy compression for three-dimensional adaptive mesh refinement simulations," in *Proceedings of the 31st In*ternational Symposium on High-Performance Parallel and Distributed Computing, 2022, pp. 135–147.
- [46] X. Liang, S. Di, D. Tao, Z. Chen, and F. Cappello, "An efficient transformation scheme for lossy data compression with point-wise relative error bound," in 2018 IEEE International Conference on Cluster Computing (CLUSTER). IEEE, 2018, pp. 179–189.
- [47] S. Jin, J. Pulido, P. Grosset, J. Tian, D. Tao, and J. Ahrens, "Adaptive configuration of in situ lossy compression for cosmology simulations via fine-grained rate-quality modeling," in *Proceedings of the 30th International Symposium on High-Performance Parallel and Distributed Computing*, 2021, pp. 45–56.
- [48] M. Davis, G. Efstathiou, C. S. Frenk, and S. D. White, "The evolution of large-scale structure in a universe dominated by cold dark matter," *The Astrophysical Journal*, vol. 292, pp. 371–394, 1985.
- [49] B. Fang, D. Wang, S. Jin, Q. Koziol, Z. Zhang, Q. Guan, S. Byna, S. Krishnamoorthy, and D. Tao, "Characterizing impacts of storage faults on hpc applications: A methodology and insights," in 2021 IEEE International Conference on Cluster Computing (CLUSTER). IEEE, 2021, pp. 409–420



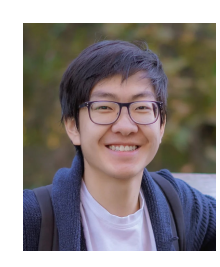
Daoce Wang is a PhD student in Intelligent Systems Engineering at Indiana University Bloomington. He received his bachelor's degree in Computer Science from University of Electronic Science and Technology of China in 2018 and his master's degree in Computer Science from University of Florida in 2020. His research interests include scientific data reduction, AMR simulations, and parallel algorithms. Email: daocwang@iu.edu.



Jesus Pulido is a research scientist in the Data Science at Scale Team at Los Alamos National Laboratory. Pulido received his Ph.D. in Computer Science at University of California, Davis in 2019. Pulido specializes in data analysis, data reduction, visualization, high performance computing, wavelets and multi-resolution methods. He has experience in applications of image sensors, astronomy, turbulence and cosmology. Email: pulido@lanl.gov.



Pascal Grosset is a scientist in the Data Science at Scale team at Los Alamos National Laboratory. His primary research interests are large-scale data analysis and visualization, and data reduction. He received his Ph.D. in Computing: Graphics and Visualization from the University of Utah in 2016 where his research focused on large scale visualization. Email: pascalgrosset@lanl.gov.



Sian Jin is an assistant professor at Temple University. He received his Ph.D. in Computer Engineering from Indiana University in 2023 and B.S. in Physics from Beijing Normal University in 2018. His research interests include high performance computing, data compression, neural networks, and parallel computing. He has published several papers in major journals and international conferences including the SC, PPoPP, VLDB, EuroSys, HPDC, IPDPS, and ICDE. Email: sianjin@iu.edu.



Jiannan Tian is a PhD candidate in Intelligent Systems Engineering at Indiana University Bloomington. His research interests include lossy compression for scientific data and error analysis, and GPU-centric computing. His ongoing project including developing GPU-accelerated compression algorithm and system design optimization of lossy compression. Email: jti1@iu.edu.



Kai Zhao is an assistant professor of computer science at Florida State University. He received his Ph.D. in computer science from University of California, Riverside in 2022. He received his bachelor's degree from Peking University in 2014. His research interests include high-performance computing, scientific data management and reduction, and resilient machine learning. Email: kzhao@cs.fsu.edu.



James P. Ahrens received the BS degree in computer science from the University of Massachusetts at Amherst in 1989, and the PhD degree in computer science from the University of Washington at Seattle in 1996. He is a senior scientist at Los Alamos National Laboratory. His primary research interests include visualization, computer graphics, data science, and parallel systems. He is author of more than 100 peer reviewed papers and the founder/design lead of ParaView, an open-source visualization tool designed to handle extremely large data. ParaView is broadly

used for scientific visualization and is in use at supercomputing and scientific centers worldwide. He is the chair of the IEEE Computer Society Technical Committee on Visualization and Graphics (TCVG). Email: ahrens@lanl.gov.



Dingwen Tao is an associate professor at Indiana University Bloomington, where he directs the High-Performance Data Analytics and Computing Lab. He received his Ph.D. in Computer Science from University of California, Riverside in 2018 and B.S. in Mathematics from University of Science and Technology of China in 2013. He is the recipient of various awards including NSF CAREER Award (2023), Amazon Research Award (2022), Meta Research Award (2022), R&D100 Awards Winner (2021), IEEE Computer Society TCHPC Early Career Re-

searchers Award for Excellence in HPC (2020), NSF CRII Award (2020), and IEEE CLUSTER Best Paper Award (2018). He is serving as an Associate Editor of IEEE Transactions on Parallel and Distributed Systems. He is a senior member of IEEE and ACM. Email: ditao@iu.edu.